Journal of Colloid and Interface Science 678 (2025) 518–533

Contents lists available at ScienceDirect

Journal of Colloid And Interface Science

journal homepage: www.elsevier.com/locate/jcis

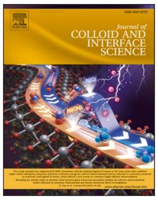

Regular Article

Enhancing deep visible-light photoelectrocatalysis with a single solid-state synthesis: Carbon nitride/TiO_2 heterointerface

Ingrid F. Silva [a], Carolina Pulignani [b], Jokotadeola Odutola [c], Alexey Galushchinskiy [a], Ivo F. Teixeira [a,d], Mark Isaacs [e,f], Camilo A. Mesa [g], Ernesto Scoppola [h], Albert These [i,j], Bolortuya Badamdorj [a], Miguel Ángel Muñoz-Márquez [k], Ivo Zizak [l], Robert Palgrave [e,f], Nadezda V. Tarakina [a], Sixto Gimenez [g], Christoph Brabec [i,m], Julien Bachmann [n], Emiliano Cortes [o], Nikolai Tkachenko [c], Oleksandr Savateev [a], Pablo Jiménez-Calvo [a,n,o,1,*]

[a] *Department of Colloid Chemistry, Max-Planck-Institute of Colloids and Interfaces, Am Mühlenberg 1, 14476 Potsdam, Germany*
[b] *Yusuf Hamied Department of Chemistry, University of Cambridge, Cambridge, United Kingdom*
[c] *Faculty of Engineering and Natural Sciences, Tampere University, P.O. Box 541, Tampere, 33101 Finland*
[d] *Department of Chemistry, Federal University of São Carlos, 13565-905, São Carlos, SP, Brazil*
[e] *HarwellXPS, Research Complex at Harwell, Rutherford Appleton Lab, Didcot OX11 0FA, United Kingdom*
[f] *Department of Chemistry, University College London, 20 Gower Street, London, WC1H 0AJ, United Kingdom*
[g] *Institute of Advanced Materials (INAM), University Jaume I, 12006 Castello de la Plana, Spain*
[h] *Department of Biomaterials, Max Planck Institute of Colloids and Interfaces, Am Mühlenberg 1, 14476 Potsdam, Germany*
[i] *Institute of Materials for Electronics and Energy Technology (i-MEET), Friedrich-Alexander-Universität Erlangen-Nürnberg, Martensstrasse 7, 91058 Erlangen, Germany*
[j] *Friedrich-Alexander-Universität Erlangen-Nürnberg (FAU), Erlangen Graduate School in Advanced Optical Technologies (SAOT), Paul-Gordan-Str. 6, 91052 Erlangen, Germany*
[k] *Chemistry Division, School of Science and Technology, University of Camerino, Via Madonna delle Carceri, Italy*
[l] *Helmholtz-Zentrum Berlin für Materialien und Energie, Albert-Einstein-Str. 15, 12489 Berlin, Germany*
[m] *Helmholtz-Institute Erlangen-Nürnberg (HI ERN), Immerwahrstraße 2, 91058 Erlangen, Germany*
[n] *Chemistry of Thin Film Materials, IZNF, Friedrich-Alexander-Universität Erlangen-Nürnberg, Cauerstraße 3, 91058 Erlangen, Germany*
[o] *Nanoinstitute Munich, Faculty of Physics, Ludwig-Maximilians-Universität München, Königinstraße 10, 80539, München, Germany*

GRAPHICAL ABSTRACT

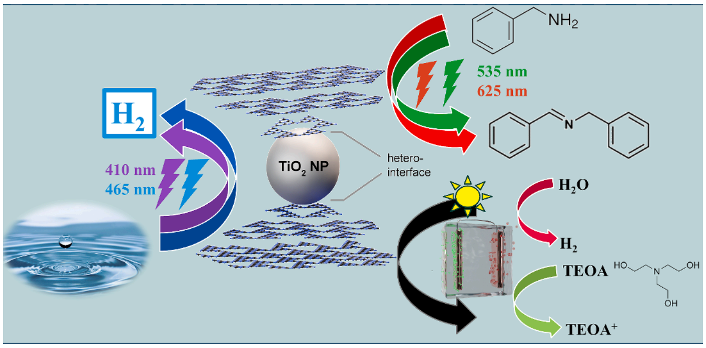

---

* Corresponding author.
E-mail addresses: pablo.jimenez-calvo@mpikg.mpg.de, pablo.jimenez.calvo@fau.de (P. Jiménez-Calvo).

[1] Present addresses.

https://doi.org/10.1016/j.jcis.2024.09.028
Received 22 May 2024; Received in revised form 29 August 2024; Accepted 3 September 2024

ARTICLE INFO

Keywords:
TiO_2 sensitization
Heterointerface
CN-TiO_2 composite
Benzylamine photooxidation
Hydrogen production

ABSTRACT

Visible-light responsive, stable, and abundant absorbers are required for the rapid integration of green, clean, and renewable technologies in a circular economy. Photoactive solid–solid heterojunctions enable multiple charge pathways, inhibiting recombination through efficient charge transfer across the interface. This study spotlights the physico-chemical synergy between titanium dioxide (TiO_2) anatase and carbon nitride (CN) to form a hybrid material. The CN(10%)-TiO_2(90%) hybrid outperforms TiO_2 and CN references and literature homologs in four photo and photoelectrocatalytic reactions.

CN-TiO_2 achieved a four-fold increase in benzylamine conversion, with photooxidation conversion rates of 51, 97, and 100 % at 625, 535, and 465 nm, respectively. The associated energy transfer mechanism was elucidated. In photoelectrochemistry, CN-TiO_2 exhibited 23 % photoactivity of the full-spectrum measurement when using a 410 nm filter. Our findings demonstrate that CN-TiO_2 displayed a band gap of 2.9 eV, evidencing TiO_2 photosensitization attributed to enhanced charge transfer at the heterointerface boundaries *via* staggered heterojunction type II.

1. Introduction

Photoelectrocatalysts for powering solar-driven chemical reactions need to effectively capture a broad range of sunlight, including visible photons, and generate electron-hole pairs with sufficient lifetimes to diffuse and initiate catalytic reactions with reasonable quantum yields while preventing back reactions. [1].

Titanium dioxide (TiO_2), an archetypical photocatalyst, is the most widely studied semiconductor (SC) for photocatalytic reactions due to its high activity, particularly its strong oxidation potential. [2,3] Unfavorably, TiO_2 has a wide band gap that limits solar spectrum utilization and has fast recombination kinetics. [4] For those reasons strategies like doping, [5] single-atom anchoring, [6] nanostructuring, [7] photonic engineering, [8] adding surface plasmons, [9] surface functionalization or passivation, [10] facet modulation, [11] and mesoporous structures, [12] co-catalysts, [13] and heterojunctions [14] have been applied to address these drawbacks. [4].

Heterojunctions are interfaces between two distinct SCs, which are versatile hybrid materials in photo- and electro-catalysis. [15] They enable the precise control of charge carrier flows, govern electron transport, define surface physics events, manage interfacial transport processes, and guide electron directions at the boundaries. [16] This fosters the rational design of chemical reactions and, combined with these benefits, they greatly enhance the efficiency in environmental and energy-related processes and devices. Analogous to the photocatalytic mechanism in SCs systems, where the SC carries out both light absorption and charge transport, [17] in a heterojunction, a sensitizer (medium or small band gap SC) absorbs light, [18] and charge separation occurs across the interface formed. This separation happens when electrons, generated by photo-excitation in the conduction band (CB) of the sensitizer (medium band gap SC, CN), are potentially injected into the CB of the wide band gap SC, TiO_2. [19] In fact, this sensitization effect was elucidated in dye-sensitized solar cells, [20] using organic dyes in contact with a mesoporous TiO_2-based multijunction with a femtosecond (fs) to sub-picosecond (ps) charge transfer rate to capture light and generate electricity. [12,19,21].

Engineering a heterointerface consists of using a medium or small band gap SC2 in intimate contact with a wide-band gap SC1 such as TiO_2. [22]) Particularly, CN exhibits key benefits when forming the CN-TiO_2 heterointerface [23,24]; offering the photosensitization effect by extending TiO_2 light-absorption to the visible range to further exploit the use of solar spectrum, and improved charge transfer kinetics. Consequently, numerous electrode-engineered catalysts, denoted as CN_x-MO_x (where M is any metal forming a stable oxide), have been developed. [23,25–32] The CN_x-MO_x system offers two key advantages: a) extending oxide light absorption, and b) enabling new charge transfer pathways. These improvements enhance two critical aspects of an active semiconductor: photon generation and diffusion. However, these systems have been studied under white light or with cut-off filters, which limits the precise evaluation of their performance under monochromatic light.

The single wavelength performance analysis offers advantages: it enables precise photoexcitation to distinguish wavelength specific phenomena, and determines the photon absorption percentage in a narrow energy range. [33,34] Consequently, single wavelength photoelectrocatalysis offers a step forward to the next generation of visible-light responsive hybrids. [35,36] Literature studies indicate a few bottlenecks, typical synthesis entails multiple steps, a technical limitation for high-throughput implementation or scaling up. [37,38] Bulk or thin film methods are commonly used, often accompanied by pre- or post-thermal treatments. Regarding the standard photocatalysis protocol, one large drawback is the use of considerable concentrations of non-recyclable sacrificial agents and high loadings of a co-catalyst, resulting in increased costs, environmental impact due to waste generation, and toxicity concerns. [15,39] Given the complexity of material preparation and testing, evaluating visible-light responsive SCs under specific monochromatic light is critical to developing new technologies.

The theoretical band edges of TiO_2 and CN are misaligned, thus forming a staggered type II heterojunction as depicted in Fig. 1 [40] In type II heterojunction, the CB of CN is above that of TiO_2, while conversely the valence band (VB) of the TiO_2 is below that of CN. This band offset creates multiple charge carrier paths, promoting efficient charge separation with ease to diffuse, available in the surface to facilitate surface redox reactions. In this heterojunction, electrons and holes move in opposite directions: photoexcited electrons in the CB of CN migrate to the CB of TiO_2, and TiO_2 photogenerated holes in its VB migrate to the VB of CN. [41] In fact, fs-transient absorption [42] and diffuse [43] spectroscopies have detected rapid charge transfer in homogeneous and heterogeneous CN-TiO_2 systems with 1 and a few tens of ps, respectively.

Organic photocatalysis, an emerging research area, is a versatile tool with potential to address current challenges in organic chemistry while adopting environmental practices. [44] Oxidative organic photocatalysis is an emerging sub-field with proven promise. [44] Its attractiveness relies on converting substrates by photon activation into added value chemicals. In fact, oxidative photocatalysis converts benzylamine to dibenzylimine, a highly valuable chemical. Imines and their derivatives are vital for building heterocycles and linear units like imidazoles, palladacycles, oximes, and hydrazones, constituting a market worth of 1 billion EUR. [45] The common industrial organic synthesis uses platinum (Pt), aluminum, nickel, or copper catalysts that require multiple step reactions. Despite this approach being scalable and of high-yield, it is also time-intensive, costly, and unsustainable. In contrast, photocatalysis offers a path to comparable imine yields with a greener and simpler method *via* photoinduced energy transfer based on sustainable catalyst materials.

Photo(electro)chemistry (PEC) offers a reliable and well-established evaluation method used with immobilized catalysts. [46] By anchoring the catalyst onto an electrode, its separation from the reaction medium is ensured, allowing to conduct studies of aqueous reactions of amines, alcohols, or water. [1,15,47,48] Presently, pH-dependent state-of-the-art catalysts for the particular case of water oxidation PEC predominantly consist of iridium, ruthenium, and other oxides. [49–51] These metallic components have significant drawbacks that diminish their suitability as scalable technology, including limited availability, high costs, potential raw material shortages for scaled production, and susceptibility to dissolution. Like PEC, efficient photocatalytic hydrogen (H_2) evolution (HER) is of great importance, [52,53] and the most effective catalyst for this purpose is $SrTiO_3$:Al material. [54] However, the preparation of this catalyst involves multi-step protocols, high temperatures, and UV photon activation, creating opportunities for solutions. [55].

Hybrid carbon-interface composites offer a promising strategy to reduce dependence on pure metal oxides. [33] Selective amine and alcohol oxidations represents an opportunity to streamline chemical processes, [56] generating added-value intermediates for pharmaceuticals, polymers, vitamins, fragrances, and various industries. [57].

To advance the rational design of visible light absorbers for controlled ratio photocatalysis and photoelectrocatalysis [33], this study investigated TiO_2 sensitization by adding melamine blended with commercial TiO_2 anatase nanoparticles (NPs) at a defined initial ratio. This blend facilitates the formation of a heterojunction during thermal polycondensation, guided by an existent mathematical model accounting for CN growth and stoichiometry. The resulting CN-TiO_2 (10–90 wt %) hybrid, along with bare and calcined TiO_2 and CN references, were studied and compared using benzylamine photooxidation, utilizing single-wavelength deep visible (red and green light) activation – a first in literature, to our knowledge, along with elucidation of the energy transfer mechanism. Additionally, photocatalytic HER, PEC triethanolamine (TEOA) and methanol (MeOH) oxidation tests were also conducted under visible light to provide further evidence of TiO_2 sensitization.

2. Results and discussion

2.1. Single solid-state CN growth on TiO_2 NPs

Fig. 2a depicts the single solid-state step used for synthesizing the hybrid CN-TiO_2 material. The solid-state thermal polycondensation method uses commercial TiO_2 anatase and melamine in defined ratios as starting materials, following an established mathematical method described elsewhere. [23] The polycondensation reaction was conducted under an inert atmosphere to prevent oxidation to the oxide phase.

To understand the structure-performance relationship, it is essential to fully characterize the CN structure. The thermal stability of CN is typically linked to its semi-crystalline nature, which is associated with factors such as the length of its polymeric chains, the ratio of its two fundamental units (s-triazine and tri-s-triazine, also known as heptazine), and its bulk thickness. [58] To that end, TGA profiles (Fig. 2b) help to understand the kinetics of the decomposition events of CN materials and to acquire the percentage of CN_x and TiO_2.

In the CN-TiO_2 composite, the mass loss originates from the organic rather than the inorganic phase. The TiO_2 references did not decompose in the thermal study range (50–900 °C) evidencing their high thermal stability. The CN reference (Fig. 2b inset) derivative shows a mono exponential decomposition, starting at 560 °C, and ending with a drastic decay at 760 °C. The CN-TiO_2 (Fig. 2c) exhibited a 2.5 % weight loss below 300 °C, attributed to adsorbed H_2O species. This loss was not factored into the 10 % organic phase. The decomposition profile reveals two distinct events: a quasi-linear broad peak spanning from 325 to 535 °C ($\Delta T=210$ °C), followed by a more rapid exponential decay peak from 535 to 650 °C ($\Delta T=115$ °C). The second peak in CN-TiO_2 decomposition reached its maximum at 565 °C. The first decomposition rate was slower than the second, suggesting the presence of two distinct polymeric chains entangled to the TiO_2 NPs.

Moreover, the CN-TiO_2 composite and CN reference display different TGA decomposition profiles, leading us to conclude that the type of CN from the composite and the bulk reference are of a different nature. An experimental proof is the maximal decomposition temperatures observed at 565 °C for CN-TiO_2 and 730 °C for CN, showcasing differing thermal stabilities in line with literature on CN materials. [59–61].

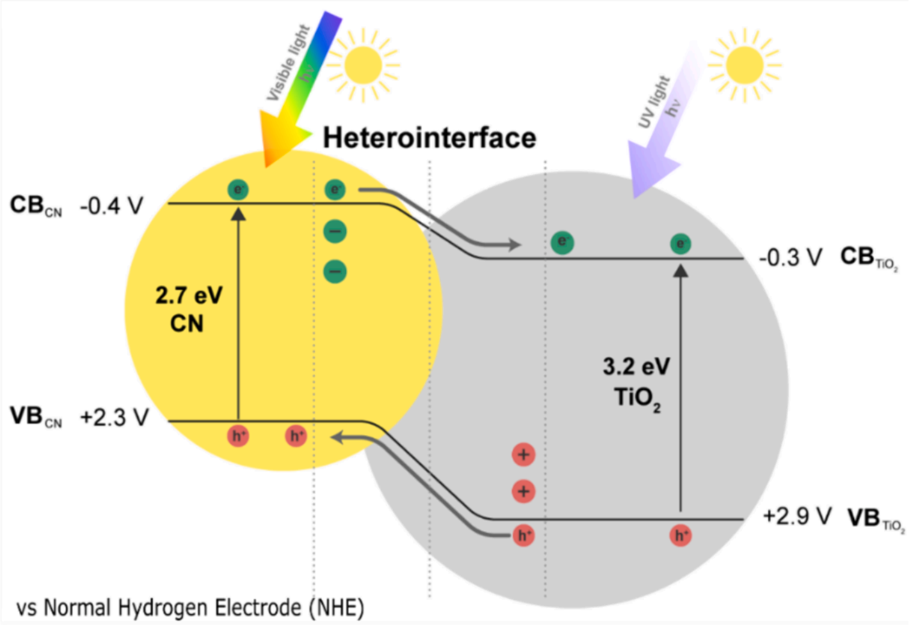

Fig. 1. Heterointerface from coupling CN and TiO_2 with their respective band gaps, CB, and VB edges, and charge carrier transfer possibilities, as postulated for heterojunction type II staggered.

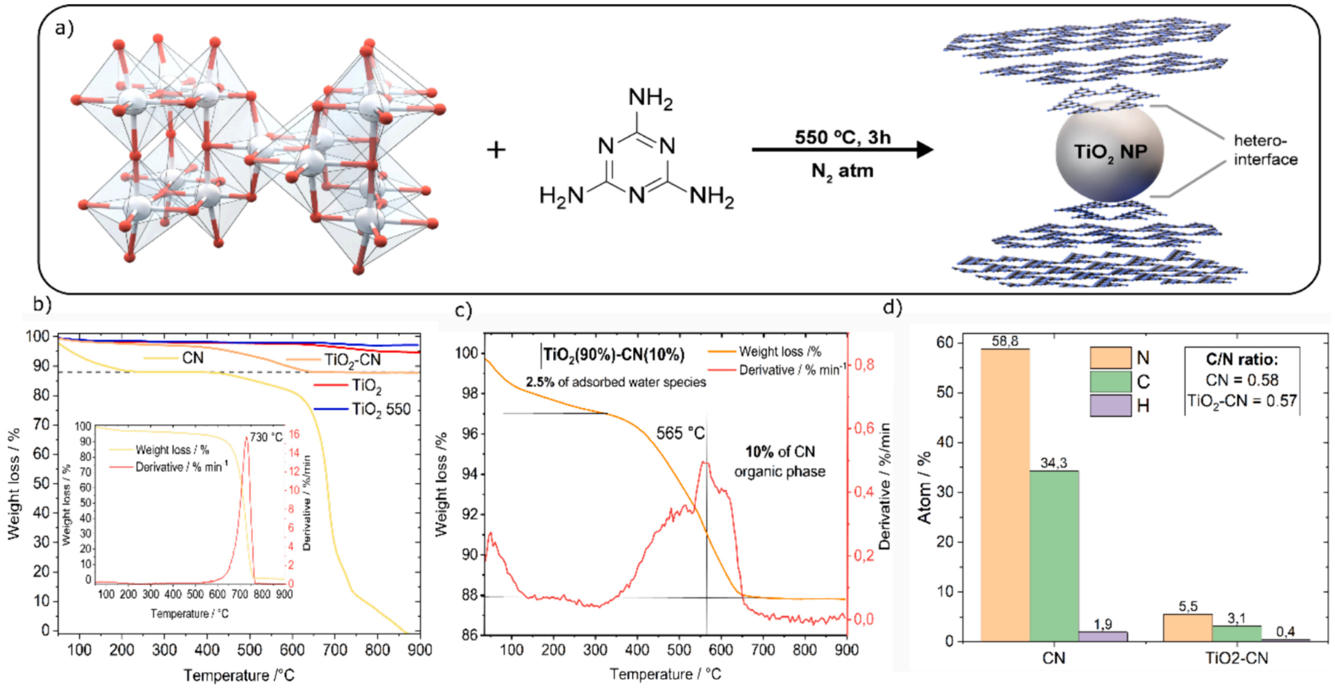

Fig. 2. a) Synthetic scheme to obtain the CN-TiO_2 composite following thermal polycondensation. b) TGA profiles for all as-prepared samples. inset) Derivative of weight loss of the CN reference. c) TGA profile and derivative of the CN-TiO_2 composite. d) Elemental analysis of the two organic based-samples, CN reference and CN-TiO_2 composite.

The two observed decomposition events in the CN-TiO_2 composite profile allow us to hypothesize that two different sizes of CN layers are formed. We hypothesize that TiO_2 facilitates the oxidation of the CN to some extent, which would explain the two decomposition events observed. In the proposed model, the CN sheets close to TiO_2 surface are smaller due to increased network disruption, while CN layers further from the TiO_2 NPs are allowed to grow larger with no interferences from the titania, as illustrated in Fig. 2a. The second hypothesis involves that intimately adhered CN sheets are likely tilted and contribute to a modest entanglement (second decomposition contribution) over the TiO_2 NPs – with covalent bonding between both phases, whereas the CN sheets at further distances are less contorted but instead flat and therefore more exposed, and thermally less stable (first slower decomposition contribution). The CN coverage over the TiO_2 NPs is neither complete nor homogeneous.

The elemental analysis results (Fig. 2d) reinforce the effective formation of CN in the composite, since the C/N ratio is equal to the CN reference, *ca.* 0.57. The carbon and nitrogen atomic percentages demonstrate that the CN-TiO_2 composite consists of 10 % CN, consistent with the deduction from the TGA derivative.

Fourier transform infrared (FT-IR) attenuated total reflectance spectra (Fig. S1) show the characteristic peaks of CN in both the CN-TiO_2 composite and CN reference. The peaks between 1620 and 1230 cm^{-1} were ascribed to the heptazine fingerprint, with a detailed attribution of those peaks discussed by Jiménez *et al.* [60] CN-TiO_2 shows heptazine signals, though attenuated compared to the CN reference, indicating the presence of $\leq$ 10 % CN at the TiO_2 interface. TiO_2 samples, on the other hand, do not exhibit these signals.

2.2. Optoelectronic characterization

To investigate the key optoelectronic properties of the CN-TiO_2 composite, we analyzed its optical and electronic features *via* UV–vis, photoluminescence (PL), and Mott-Schottky electrochemical measurements.

The prepared powder materials exhibited differing colors (Fig. 3a); CN-TiO_2 composite appears as a light orange, graphitic CN reference as a reddish-orange, and the bare and calcined TiO_2 references as white.

The Kubelka-Munk function [62] displayed the UV–vis diffuse reflectance spectra (Fig. 3b), revealing the anticipated onset of absorption for TiO_2 and CN reference materials at 375 nm and 460 nm, respectively. Interestingly, the CN-TiO_2 composite displayed a pronounced red shift compared to TiO_2-based materials. The CN contribution in the CN-TiO_2 composite differs from the CN reference in two ways: a) the absence of the typical maximum peak band found in CN at 410 nm, and b) a red-shifted tail in its absorption, with a gradual decay starting at the characteristic TiO_2 indirect band edge, *ca.* 388 nm. [63].

Band gap values were determined using the Tauc relation (Fig. 3c, Table 1) [64]: 2.9 eV for CN-TiO_2 composite, 2.7 eV for CN, 3.3 eV for both TiO_2 550 and bare TiO_2. After analysis of the CN-TiO_2 composite, a noticeable tail extending from 388 to 650 nm into the visible spectrum is seen, attributed to the undeniable presence of CN. This tail displays multiple slopes due to the aggregation of smaller band gaps, reflecting the heterogeneous nature of the material. [33,65,66] The 2.9 eV band gap implies TiO_2 sensitization upon CN incorporation and interface formation, consistent with the literature. [16,23,60,67,68,9].

Fig. S2 shows the drop cast film absorbances on FTO calculated from transmittance acquired with an integration sphere (equivalent to the electrodes used in PEC). The additional UV–vis measurements were conducted to compare the absorption of thin film samples, consistent with powder analysis Fig. 3c.

The steady state PL analysis of the powder thin films, cast on FTO substrates (equivalent to the electrodes used in PEC), were conducted across various excitation wavelengths, *i.e.*, 320, 380 (Fig. S3a-b), 400 (Fig. 3d), and 465 nm (Fig. S3c). This allowed us to understand the electronic transitions and dynamics of charge carriers. Though the samples were deposited on FTO, we exclude the term 'FTO' in the text for simplicity.

The clear PL peaks observed in the CN across the studied wavelengths are attributed to the excitonic PL signal, from $\pi^* \rightarrow n$ and $\sigma^* \rightarrow n$ electronic transitions driven by the lone pair of electrons in nitrogen. [69,70] This PL onset is associated with band-to-band PL signals. [71]

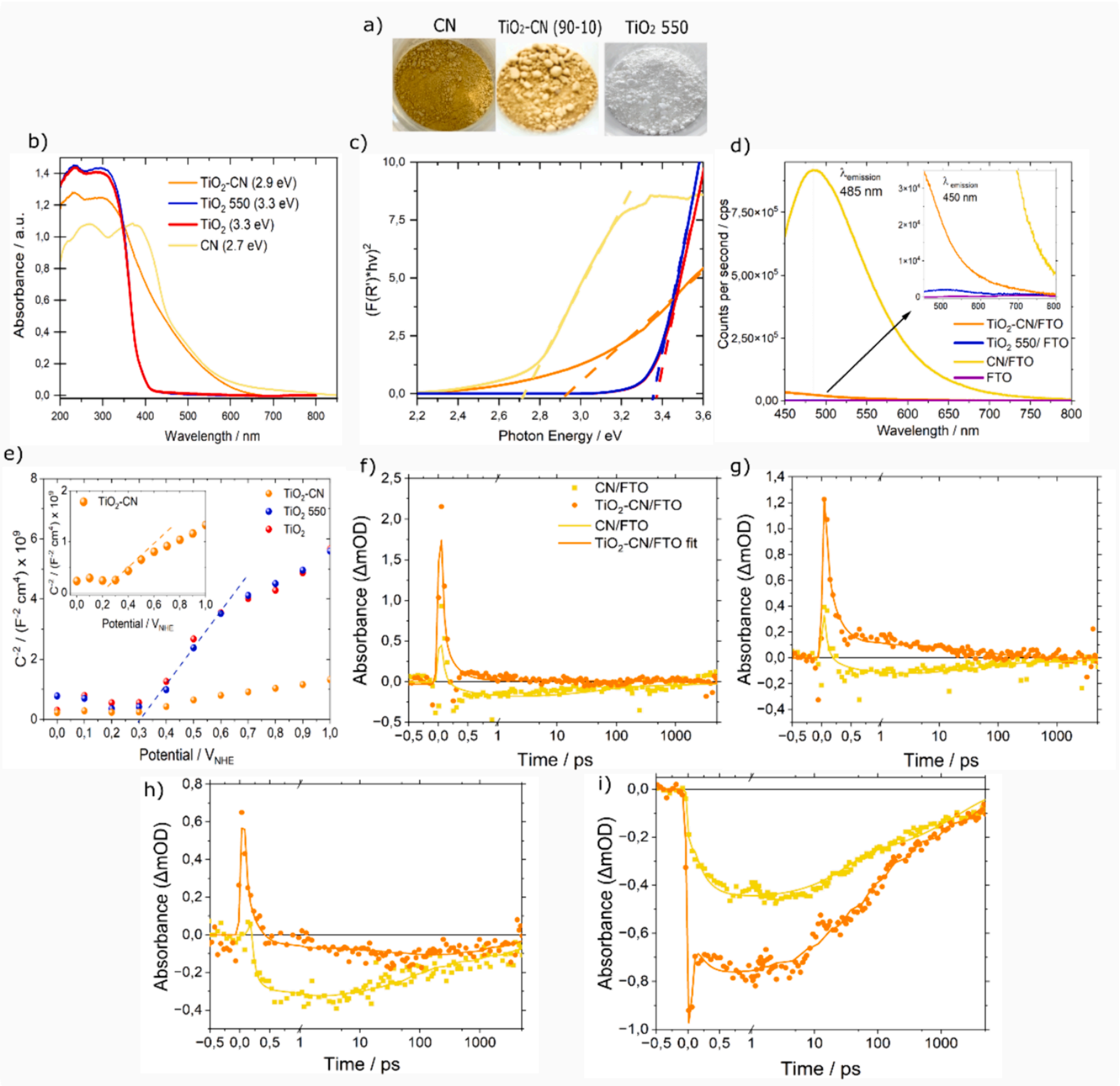

Fig. 3. a) picture of the material powders color of the hybrid cn-tio$_2$ composite and the two references: CN and calcined TiO$_2$. b) UV–vis spectra and c) Tauc plot of CN-TiO$_2$ composite, TiO$_2$ 550, TiO$_2$, and CN samples. d) Steady-state PL spectra of the powder thin film at 400 nm excitation. e) Mott-Schottky plot. Comparison of the TA decays of the CN-TiO$_2$ composite and CN reference excited at 400 nm at monitoring wavelengths of f) 500 nm, g) 600 nm, h) 700 nm, and i) 1000 nm (excitation density 0.1mJ/cm^2).

Table 1

Band gap, surface area, pore size, and anatase crystallite size of the as-prepared materials.

Sample	BG^T / eV	Surface area / m^2/g	Average pore size / nm	Anatase (101) / nm
TiO$_2$	3.3 ± 0.1	85 ± 8	5.3 ± 0.5	21.9 ± 0.1
TiO$_2$ 550	3.3 ± 0.1	65 ± 6	6.5 ± 0.6	24.4 ± 0.2
CN-TiO$_2$	2.9 ± 0.1	49 ± 5	3.8 ± 0.4 / 5.3 ± 0.5	22.1 ± 0.1
CN	2.7 ± 0.1	33 ± 3	3.8 ± 0.4	n.d.

Conversely, TiO$_2$ is known as an indirect band gap semiconductor with high photoactivity, resulting in a low PL quantum yield on its own. [63] Therefore, the PL signal detected in the CN-TiO$_2$ composite can be solely attributed to the contribution of the CN transitions. This additional indication confirms the successful formation of an intimate heterointerface.

Interestingly, in the excitation wavelength range of 320 to 465 nm, the emission onset of the CN reference and the CN-TiO$_2$ composite shifted from 475 and 440 nm to 510 and 545 nm, respectively. These emission shifts can be attributed to variations in the absorption due to the coexistence of CN sheets of different sizes and to microstructural differences [70], in agreement with TGA (Fig. 2c) and as reported elsewhere. [71] Moreover, the effect of TiO$_2$ NP scaffold cannot be ruled out. In the CN-TiO$_2$ composite, we propose a hypothesis suggesting a scenario in which the smaller CN sheets primarily undergo σ*→ n transitions as a radiative pathway. [70] This theoretically translates in a broader band gap and, consequently, a more pronounced blue shift, contrarily with the CN reference. It is presumed the CN reference contains larger (and possibly more conjugated) CN sheets mainly undergoing π*→n transitions, leading to absorbance at longer wavelengths. The larger CN sheets in the reference exhibit more nonplanar sites, breaking symmetry and allowing for these transitions. [72] However, at 465 nm excitation, there was a noticeable red shift in the CN-TiO_2 composite's emission onset compared to its CN reference.

Qualitative analysis of the emission intensity reveals a quenching effect of 10–100 times higher for CN-TiO_2 compared to CN. During PL quenching, when trap states are present, the emission is quenched because trapping competes with the radiative decay process. [73] This quenching effect, has been previously identified in analogous systems. [42,71,74] It arises from a charge transfer mechanism from CN to TiO_2 in the composite, reducing the number of electrons available for radiative relaxation in CN. This quenching may also indicate an effective generation of separated charge carriers through photo-excitation, [41,75] implying a reduction in the density of trap states at the interfacial heterointerface of the two SCs. Another heterointerface hypothesis to consider is the influence by occupying trap states, as depicted by the band bending shown in Fig. 1. The significance of this quenching arises from the inhomogeneity of the films, which results in slight differences in absorbances between CN-TiO_2 and CN casted on FTO, as depicted in Fig. S2a.

The Mott-Schottky plot (Fig. 3e) exhibits positive slopes for all the TiO_2-based samples, indicating their *n*-type nature. [41,51,73] Merely qualitatively, the less steep slope of the CN-TiO_2 composite suggests a slightly higher carrier density compared to its TiO_2 references. While the carrier density was particularly high for these materials, the values resemble those of FTO. The determined flat band potentials were translated as CB values for the photoelectrodes. The CN-TiO_2 composite and TiO_2 references displayed 0.2 V and 0.3 V vs NHE, respectively. This indicates that CN inclusion has a slight influence on TiO_2's electronic band structures, consistent with prior research. [23].

2.3. *Charge carrier dynamics by transient absorption spectroscopy*

Femtosecond transient absorption spectroscopy (fs-TAS) is a highly sensitive method for examining the dynamics of charge carriers, [76] encompassing carrier formation and recombination mechanisms. It is used here to gather insight into the charge transfer mechanisms of the heterojunctions through changes in transient absorption (TA) responses of the as-prepared samples. fs-TAS was measured on thin films drop casted onto FTO substrate, which is equivalent to the electrodes used in PEC. Different excitation wavelengths were used, further details on the strategy of the analysis are found in Section S2. Despite the samples being deposited on FTO, we exclude the term "FTO" in the discussion for simplicity.

The fs-TAS studies were complemented by emission decay measurements using the time-correlated single photon counting (TCSPC, Section S3). However, despite 10–100 times PL quenching seen in the CN-TiO_2 composite relative to the CN reference by steady PL results (Fig. 3d), there was no marked difference in the TCSPC emission decay profiles between the CN and CN-TiO_2. It is believed that the quenching happened faster than the TCSPC's time resolution of 60 ps. Therefore, fs-TAS study main focus was on the charge transfer dynamics within the ps to sub-ps time domain.

A comparison between the CN-TiO_2 composite and CN reference TA decay profiles at 400 nm excitation, monitored at different wavelengths is shown in Fig. 3f–i. 400 nm excitation was used because only CN is expected to be excited at this wavelength, as explained in Section S2.1. (Note: at $\leq$ 380 nm excitation, in the composite, TiO_2 photoexcitation with electrons in the TiO_2 CB may hinder effective charge transfer).

The most notable difference between the responses in Fig. 3f–i is a rapid component present at all wavelengths for the CN-TiO_2 composite. The global data fit reveals a time constant close to the instrument response time, around 100 fs. Therefore, one can conclude that this component is faster than 100 fs. This matches the timescale of charge transfer in a homogenized CN-TiO_2 system. [42] Hypothetically, this fast charge transfer could indicate the injection of photo-generated electrons from CN's CB into TiO_2's CB. This increases the electrons-holes separation distance, stabilizes the electrons in TiO_2's CB due to a 0.1 eV difference in energy levels compared to CN CB (Fig. 1), and thus reduces electron-hole recombination time.

In a simplified scenario, the CN-TiO_2 composite includes two types of CN polymeric sheets: those directly contacting the TiO_2 particles and those well separated from them. The CN sheets in direct contact with TiO_2 would inject an electron into TiO_2 upon photoexcitation in a timescale of 100 fs or less, as per fs-TAS. These "quenched" CN sheets don't contribute to steady-state PL emission and have shorter excited state lifetime than the TCSPC time resolution. On the other hand, the CN sheets well separated from TiO_2 particles are not quenched and are detected using steady-state and time-resolved TCSPC PL measurements.

Considering the charge separation at earlier timescales for CN-TiO_2 composite with 400 nm excitation, one would anticipate a longer CN-TiO_2 lifetime compared to the CN reference. However, both sample responses had lifetimes longer than the longest delay of the used fs-TAS instrument (5 ns). An attempt to differentiate between different intermediate states by comparing TR spectra and decay-associated spectra obtained after global data fits was done. For further details on the TA spectra of the CN-TiO_2 composite and CN reference at the four excitation wavelengths, refer to Sections S2.2 and S2.3. Film responses are influenced by factors such as photoinduced changes in the refractive index, probe light interference, and film thickness. [77] These factors contribute to variations in spectral shapes among samples, and difficulty in precise conclusions.

Additional TAS spectra and TCSPC decay data (Fig. S4–S10) were analyzed at various excitation and monitoring wavelengths, along with various delay times, to cover a wider spectrum and identify components and intermediates in the materials. Further, a comparison of TA decays, including the fitted components, is provided in Tables S1-2. Further discussion of the results can be found in the supporting information.

2.4. *Morphological, textural, and structural characterization*

The general morphology of the samples was analyzed by scanning electron microscopy (SEM) (Fig. S11a, b). The images provide evidence of TiO_2 NPs sintering closely together. This sintering reinforces our hypothesis that the CN bulky material acts as a "glue" to bind the TiO_2 NPs.

The Annular dark-field (ADF) image (Fig. S11c) displays the same round TiO_2 morphology, with superposition among some of TiO_2 NPs, possibly due to sintering. This behavior may be in good agreement with the hypothesis of CN serving as glue, keeping the TiO_2 NPs together in a certain order, as already partially seen in the SEM images. TEM image (Fig. S11d) shows the typical TiO_2 roundish NPs of a few tens of nm in size, in agreement with TiO_2 550 reference (Fig. S12). The image in Fig. S11d emphasizes how the TiO_2 morphology prevailed in the CN-TiO_2 composite. The HR image clearly shows the typical d space of anatase (110) plane, *ca.* 0.324 nm, in agreement with the literature. In addition, the EDX (Fig. 4a and b) spectrum confirms the presence of Ti, O, C, and N elements, peaks from gold (Au) are present as Au grids with lacey carbon layers on top were used as TEM supports. Furthermore, EELS (Fig. 4c) show Ti L-, O K-, C K-, and N K-lines at their respective energies. EELS results confirm the presence of CN in the composite, in agreement with TGA, EA, UV–vis, PL, TAS, and EDX.

The X-Ray diffraction (XRD) patterns (Fig. S13) of the TiO_2 references and CN-TiO_2 composite exhibit the typical diffraction peaks of anatase (101) diffraction plane at $2\theta = 25.1^{\circ}$, with no significant shifts. Hence, for CN reference the graphitic or interlayer stacking of the

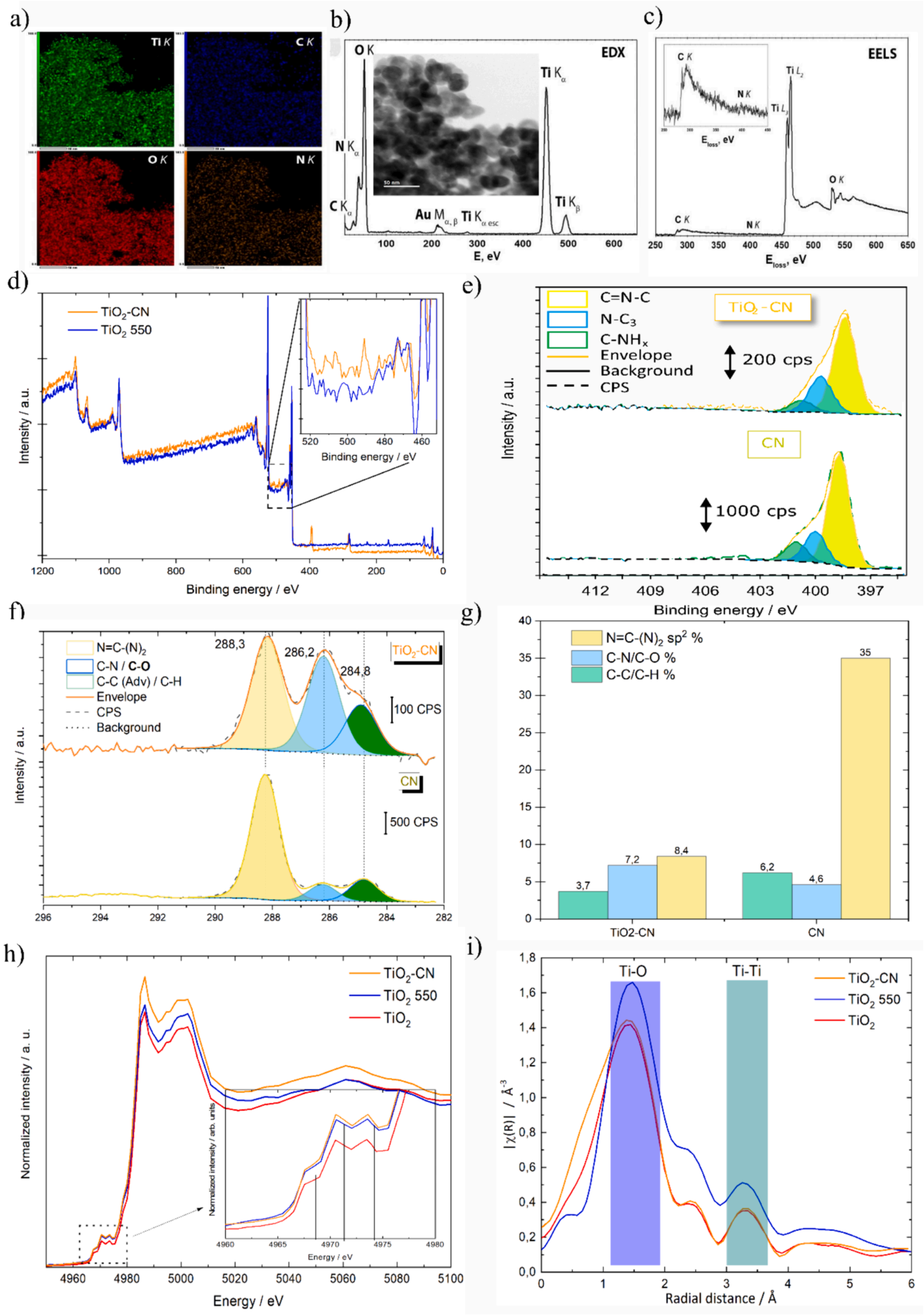

Fig. 4. a) edx element mapping distribution. b) edx associated spectra, (inset stem image). c) eels spectra. xps spectra: d) survey of the cn-tio$_2$ and TiO$_2$ 550, e) N 1 s of the CN-TiO$_2$ and CN, f) C 1 s of the CN-TiO$_2$ and CN, g) the different amount of carbon functionalities (components of the deconvolution of C 1 s XPS signal). h) XANES spectra at the Ti K-edge, (inset zoom of the pre-edge emphasizing A1-A3 and B peaks), and its i) EXAFS associated spectra.

π-conjugated aromatic system (002) plane was seen at $2\theta = 27.3^{\circ}$, and the diffraction plane for tri-s-triazine phase at $2\theta = 13.1^{\circ}$, as previously reported. [60] The lack of the 002 peak in CN-TiO_2 may stem from the nanocrystalline or amorphous nature of CNs. [78] In XRD fundamentals, very small crystallite sizes lead to significant peak broadening, complicating detection. [79] Looking at the anatase crystallite size of the TiO_2-based samples, determined by the Debye-Scherrer relationship, there was no significant difference (*ca.* 22 nm) between the composite and the bare TiO_2. However, TiO_2 calcined sample at 550 °C had an anatase crystallite size higher 24.4 ± 0.2 nm, suggesting that calcination temperature has an immediate effect on crystallinity [80], in agreement with reported studies. [81].

N_2 isotherms (Fig. S14a) of all samples exhibit type-IV isotherm and type-H4 hysteresis loop, ascribed for mesopores and slit-like pores. [82] The Brunauer-Emmett-Teller (BET) theory was used to calculate the specific surface area (S_{BET}) of the materials. All samples have relatively low surface area ($<90\ m^2\ g^{-1}$). The calcined TiO_2 at 550 °C decreases its surface area compared to bare TiO_2, suggesting that calcination disrupts the original surface of TiO_2 *via* OH dehydration, in agreement with the literature. [83] The lowest surface area was found for the CN reference ($33\ m^2\ g^{-1}$) in consistency with other polymeric CN and poly (heptazine imides) reported materials. [41,59,60] Interestingly, the hybrid CN-TiO_2 composite displayed an intermediate surface value of $49\ m^2\ g^{-1}$, suggesting the structural preservation of both materials when compared to the two references. Quenched solid density functional theory (QSDFT) was used to obtain the pore size distribution (Fig. S14b). The region with clear pores is below 10 nm. Thus, TiO_2 and CN references presented monomodal mesoporous profiles. [84] The only exception was found for the CN-TiO_2 composite with a bimodal profile. In terms of pore size, calcination of the TiO_2 sample resulted in a slight increase from 5.3 to 6.5 nm compared to the bare material. An unusual twin-pore was observed in the CN-TiO_2 composite with 3.8 and 5.3 nm pore sizes. This highlights the synergistic coexistence of pores from both TiO_2 and CN components in the hybrid composite. However, the volume capacity of its larger pore is slightly lower compared to that of the TiO_2 references.

2.5. X-ray photoelectron and absorption spectroscopies characterization

X-ray photoelectron spectroscopy (XPS) was conducted to analyze the chemical composition at the surface and use the inelastic energy to identify contributions. This aimed to reveal chemical bond details and probe local chemistry, with an emphasis on exploring the heterointerface contact of the CN-TiO_2 composite.

Comparison of the survey XPS spectra of the TiO_2 550 and CN-TiO_2 samples (Fig. 4d) may be used to identify the atomic contributions and to reveal unique topological insights into the composite structure. Normalization of the survey intensity at the titanium 2p pre-edge range (420 eV) allows us to discount inelastic scattered electrons from the C 1 s and N 1 s peaks from the carbon nitride and directly compare the post-peak range of the Ti 2p signal. In CN-TiO_2 composite, we see a clear and significant increase in the background intensity in the post-peak region (Fig. 4d inset) – indicative of an increased inelastic scatter of buried electrons. [85] Qualitative comparisons with the interface categories within the QUASES-TOUGAARD program suggest that the Ti 2p signal originates from a “d” type configuration – in which the 2p photoelectrons are located underneath an overlayer. In brief, overlayer refers to the CN layer that covers a single TiO_2 NP on the surface. No signs of buried inelastic scatter may be seen for the C and N peaks in this sample, which allows us to ascribe the spatial locale of the components of the composite as TiO_2 particles with a CN surface overlayer – rather than CN and TiO_2 existing as independent components. Thus, such finding lends evidence towards the hypothesis that these two semiconductors form a genuine interface during synthesis, in agreement with TGA, UV–vis, PL, FT-IR, EELS, and EDX.

The dominant constituents in TiO_2 550 and CN-TiO_2 materials spectra are Ti 2p (Fig. S15) and O 1 s; and if one remains consistent, it suggests that the other component also remains unaltered. As anticipated, both samples based on TiO_2 exhibited the characteristic Ti 2p contributions at 464.2 and 458.5 eV, which correspond to Ti $2p_{1/2}$ and Ti $2p_{3/2}$, respectively. [86] The quantified separation in binding energy, ∼5.7 eV, between these states is consistent with the documented Ti^{4+} state in TiO_2 anatase. [9,23].

Qualitative analysis of N 1 s and C 1 s was conducted for CN-TiO_2 and CN materials. The N 1 s signal for both samples (Fig. 4e) exhibits three equivalent deconvoluted peak contributions, a major at 401.2 eV, an intermediate at 400.1 eV, and a minor at 398.7 eV, attributed to the sp^2-hybridized pyridine nitrogen of C═N-C of the heterocyclic ring, to the tertiary nitrogen link to three carbon $N\text{-}(C)_3$, and to the terminal amino groups ($C—N—H_x$), respectively. [60,87] The characteristic sites of CN-TiO_2 composite, including $-NH_x$ and $N\text{-}(C)_3$ defects, appear in ratios comparable to the bare CN reference material, indicating that the nature and amount of defect sites have not changed significantly due to the selected preparation method.

The C 1 s signal in the CN-TiO_2 and CN materials (Fig. 4f) exhibit the equivalent three deconvoluted peak contributions but again in different proportions, a major at 288.3 eV, an intermediate at 286.2 eV, and a minor at 284.8 eV, ascribed to the sp^2-bonded C of $N{=}C\text{-}(N)_2$ from the heterocyclic ring, the C—N or C—O (evidencing the coexistence of the organic and inorganic phases with N—C—O-Ti-O interactions), and adventitious carbon or C—H groups, respectively. [60,87] The quantitative analysis of C 1 s on the study samples (Fig. 4g) reveals significant modifications in the CN-TiO_2 composite compared to the CN counterpart. Two notable increases are observed: a 64 % rise in the hetero-interface C—O interaction and a four-fold increase in C sp^2 content. Although the CN-TiO_2 composite only contains a low CN content (10 %), the size of the CN layer at the interface with each individual TiO_2 nanoparticle appears to decrease, potentially in a gradual manner. At first, the single TiO_2 nanoparticle is partially covered by a relatively small CN layer.

The analysis of the XANES Ti K-edge (Fig. 4h) aimed at comprehending local structural alterations, such as the presence of oxygen vacancies, their influence, particularly in the CN-TiO_2 interface. In spite of the availability of data points, detailed analysis was restricted. Detecting variations in Ti atom speciation and any shifts in the local environment theoretically have been accomplished through pre-edge region examination (below 4980 eV) in the TiO_2-based samples. Nevertheless, the interpretation of XANES spectra inherently involves complexities. The attribution and discussion of the pre-edge peaks (A1-A3 and B) are described in supporting information. The XANES Ti K-edge analysis indicated that no significant structural modifications occurred in the CN-TiO_2 composite compared to TiO_2, despite the CN layer entangling TiO_2. This reaffirms that the formation of the CN-TiO_2 interface does not alter the local structure or compositional environment of TiO_2, consistent with findings from XPS, EDX, EELS, EA, and BET data.

The XAS data points are limited, affecting EXAFS coordination shells analysis. The signal intensity, the EXAFS spectra Fig. 4i suggest a Ti-O distance increase, in consistency with the presence of oxygen vacancies in annealed samples as of TiO_2-550. [88,89] Indeed, obtained distances of Ti-O (1.6 Å) and Ti-Ti (3.3 Å) have been reported with similar values for TiO_2 anatase samples. [90] No notable energy shift was detected in any signals, suggesting the absence of Ti-N bonds, especially at ratios below 0.1 N/Ti. [89] This rules out nitrogen doping, as previous studies have indicated that even small amounts of *N*-doping would shift the first shell peak leftward by approximately 0.1 Ã…. [89] Additionally, the CN-TiO_2 system exhibited no significant alterations compared to the bare TiO_2 reference.

2.6. Photooxidation performance

The CN-TiO_2 composite was tested in the photooxidation of benzylamine (the substrate) to dibenzylimine (the product, Fig. 5a and S16)

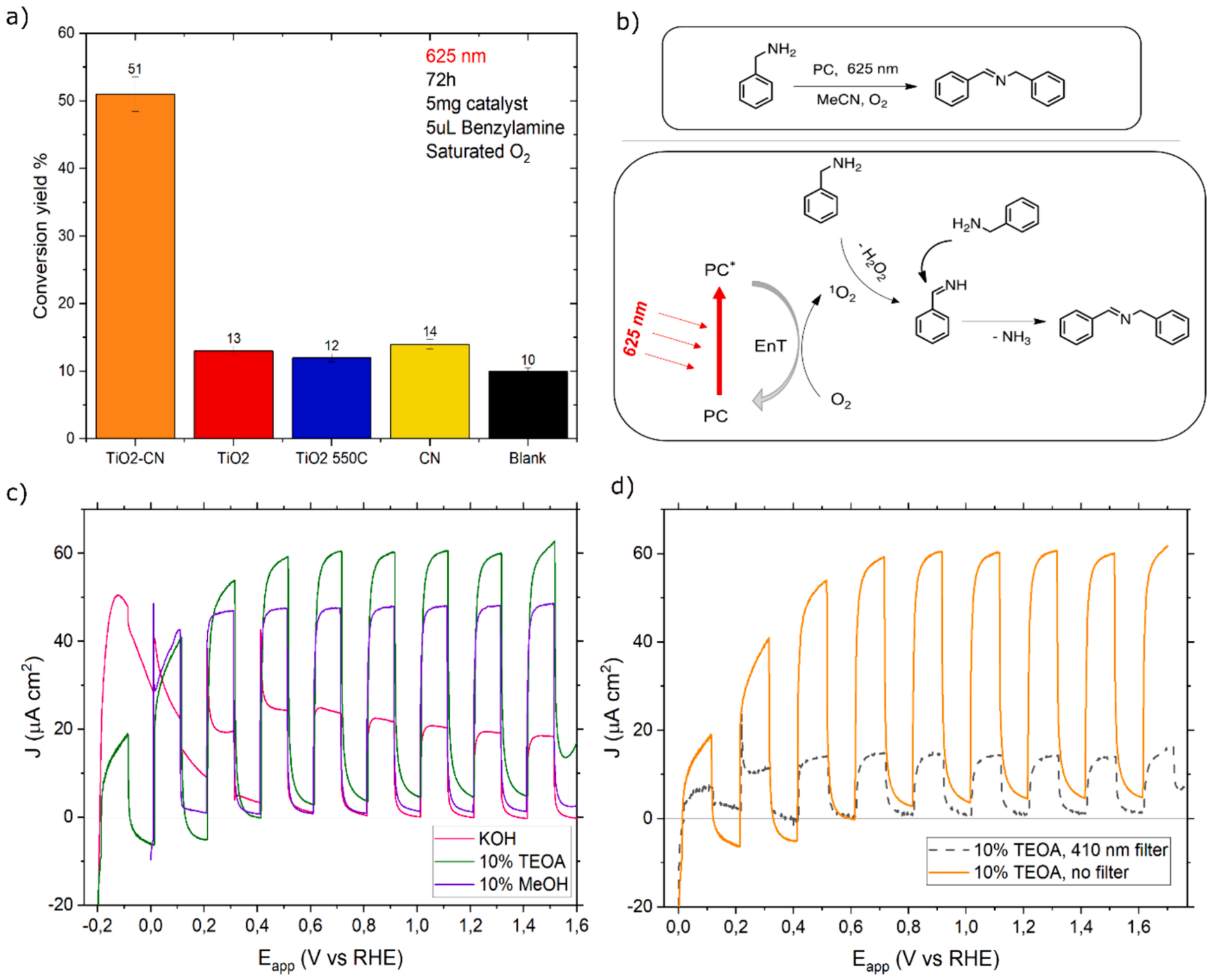

Fig. 5. a) Photooxidation of benzylamine including the reaction conditions. b) Energy transfer mechanism scheme with the associated species in the photoconversion of benzylamine to dibenzylimine. c) Linear sweep voltammetry scans of CN-TiO_2 photoelectrode (area 0.25 cm^{-2}) oxidizing three different sacrificial agents, namely KOH (pink trace), TEOA (green trace), and MeOH (blue trace). d) Linear sweep voltammetry scans of CN-TiO_2 photoelectrode with TEOA as the most efficient sacrificial agent with an applied cut-off filter applied at wavelengths lower than 410 nm, evidencing the photosensitization effect of CN within the hybrid CN-TiO_2 composite. (For interpretation of the references to color in this figure legend, the reader is referred to the web version of this article.)

upon monochromatic red, green, and royal blue-light LED irradiation at 625, 535, and 465 nm (Emissions spectra, Fig. S17), respectively to excite the series of materials. Fig. 5a shows the conversion yields of all samples. The CN-TiO_2 (10–90 %) composite demonstrated a remarkable conversion rate of 51 % yield after 72 h of reaction time. Contrarily, the blank experiment (no catalyst) with benzylamine under the same light conditions yielded only 10 %, due to the saturated oxygen atmosphere, acetonitrile, and incoming photon energy, generates oxygen-based intermediates in low proportions. Yet, these intermediates are still sufficient to convert benzylamine to imine. [91] Both the CN and TiO_2 references yield up to 14 %, which was comparable with the blank experiment, indicating no improvement. This finding underscores the TiO_2 sensitization effect, wherein CN, in close interfacial contact with TiO_2 NPs, enhances light absorption. Notably, TiO_2 exhibits poor photon absorption at a 625 nm wavelength unless coupled with a smaller SC band gap. Further data and discussion can be found in Fig. S16 at 465 nm and 535 nm, indicating that no significant differences were observed among the samples.

The energy mechanism of benzylamine photooxidation was followed by electron paramagnetic resonance (EPR, Fig. S18a-b). EPR tests allowed us to detect the formation of singlet oxygen and/or oxygen radical anions after an energy induced input. Photocatalytic benzylamine oxidation can undergo two concomitant mechanisms, namely electron and energy transfer processes. Both mechanisms involve transfer from the catalyst to the oxygen, but the former leads to the formation of an oxygen radical-anion, whilst the latter to a singlet oxygen. [92] Both reactive species can subsequently oxidize the benzylamine substrate. TEMP ($^1O_2$ radical) and DMPO (O_2 radical) were used to detect singlet and radical anion oxygen species, respectively, in dark and local illumination. The benzylamine photooxidation reaction was carried out under these conditions for 3 days, thus we opted for EPR illuminated tests with a stronger monochromatic LED light (higher energy input), 415 nm, to obtain faster confirmation of the creation of oxygen species.

Figure S18a-d displays the radical scavenger EPR tests on the CN-TiO_2 composite. The formation of TEMP – $^1O_2$ radical is confirmed by the presence of a triplet signal (Fig. S18a) illuminated *via* energy transfer to oxygen resulting in singlet oxygen formation. Similarly, the typical quadruplet signal of DMPO – $\dot{O}_2$–, confirmed the $\cdot O_2^-$ (oxygen radical anion) formation (Fig. S18b), reiterating the electron transfer to oxygen. As previously stated, the hypothesis that both types of oxygen species are generated and exist simultaneously remains applicable under these experimental conditions. Still, by comparison to prior reports, [41,91,93–95] we posit that the energy transfer mechanism prevails at 625 nm, as indicated before that this lower energy input is insufficient to induce electron transfer to O_2, as sketched in Fig. 5b.

Additionally, a comparison (Table S3) and discussion are included in the supporting information to contextualize this study among similar systems from the literature, positioning CN-TiO_2 activity as superior at deep visible light wavelengths.

2.7. Photoelectrochemical performance

To broaden the applicability of the CN-TiO_2 composite and TiO_2 reference photoelectrochemical performances were conducted in the range of −0.2 to 1.7 V vs reversible hydrogen electrode (RHE), both with (10 % v/v of TEOA and MeOH) and without a hole scavenger at pH 13 (0.1 M KOH, Fig. 5c). MeOH acts as a typical electron donor for HER and prevents O_2 formation as a common hole scavenger. TEOA serves as a strong hole scavenger, aiding in the extraction of holes on the CN to prevent recombination. [96].

In the absence of any sacrificial electron donor, the chopped linear sweep voltammetries present a non-geometric and fluctuating signal until surpassing 0.6 V vs RHE, stabilizing at a constant current density of 19 ± 2 $\mu A\ cm^{-2}$. In presence of MeOH, on the other hand, the CN-TiO_2 composite photocurrent stabilizes at a lower potential (0.2 V vs RHE), yielding a slightly higher steady-state current density of 48 ± 2 $\mu A\ cm^{-2}$ than KOH. On the other hand, with 10 % v/v TEOA, the photoanode exhibits a progressively increasing current density until reaching the highest constant value of 62 ± 3 $\mu A\ cm^{-2}$ at 0.4 V vs RHE. The initial variation in values across the three electrolytes can be ascribed to the heterogeneity of the CN-TiO_2 composite, resulting from the rough and porous CN layers in close contact with the TiO_2 NPs. When tested in KOH and TEOA, the TiO_2 reference achieved stability faster compared to the CN-TiO_2 composite (Fig. S19a). In both electrolytes, the constant current density remained at 17 ± 2 and 96 ± 10 $\mu A\ cm^{-2}$ after 0 V vs RHE. Comparing both samples, in the presence of TEOA as a hole scavenger the TiO_2 electrode outperforms the composite (Fig. 5f and S19b). KOH and TEOA, both alkaline and tertiary aliphatic bases, exhibit distinct chemical affinities. These differences influence their adsorption on the catalyst surface and result in varying oxidation potentials [39,96]. Even though CN functional groups can assist organic substrates interactions, such as MeOH and TEOA, [68] the poor electrical conductivity and limited accessibility of active sites limit the electron extraction process from the composite to the back-contact. [97].

To assess the light absorption contribution of each SC (TiO_2 and CN) in the overall photoactivity of CN-TiO_2, an additional photoelectrochemical test was conducted under a solar light simulator (Emission spectra, Fig. S20). This experiment used a 410 nm cut-off filter with two aims: a) to demonstrate visible-light photoactivity, and b) to shed light on potential electron transport paths, in the CN-TiO_2 composite by blocking photons of lower wavelengths. The TiO_2 reference voltammogram curve (Fig. S19b) displayed no photoactivity, as anticipated, given the theoretical TiO_2 band gap of 3.2 eV. Bare TiO_2 photoactivation occurs only at 388 nm or shorter wavelengths. [23] Notably, in the PEC assessment under light $\geq$ 410 nm of CN-TiO_2 curve (Fig. 5d), it retains 23 % of its photoactivity compared to the full lamp spectrum test, where only CN can absorb visible photons. The observed positive photocurrent and oxidation of TEOA (Fig. 5d) underscore the photosensitization of TiO_2. This suggests electron flow, or injection, from the CN CB to the TiO_2 CB, [67,81] as theorized in staggered type II heterojunctions. This process is facilitated by the organic/inorganic heterointerface, as depicted earlier in Fig. 1.

2.8. Photocatalytic hydrogen evolution reaction

The photoactivity and efficiency of H_2 production in the CN-TiO_2 hybrid were examined as a tertiary complementary test. This aimed to reinforce the proof-of-principle of the observed TiO_2 photosensitization effect, demonstrated by its superior activity in benzylamine photooxidation under red light (625 nm). All systems (Pt/TiO_2 550, Pt/CN, and Pt/CN-TiO_2) were tested under two wavelengths: 410 nm and 465 nm (Fig. S21a, emission spectra Fig. S22). CN-TiO_2 composite exhibited superior activity with 319 and 148 $\mu mol\ h^{-1}\ g^{-1}$ at 410 and 465 nm, respectively. Quantum yield was determined to mirror the H_2 production trend for the samples at both studied wavelengths (Fig. S21b), indicating a direct light photon absorption and activity to H_2 evolution. Insights into TiO_2 sensitization and the energy diagram of such heterogeneous system can be found in Fig. S21c. Additionally, a comparison Table S4 is included to contextualize this study among similar systems from the literature, positioning Pt/CN-TiO_2 activity as modest.

2.9. Impedance spectroscopy

Fig. S23a-c displays the values of series resistance (R_s), charge transfer resistance (R_{CT}), and capacitance of the as-prepared samples in the dark. The value of R_s (Fig. S23a) remained approximately constant within the potential range of −0.2 to 1.6 V vs RHE for all samples. Both CN-TiO_2 and TiO_2 550 samples exhibited closely matched values, indicating that the substrate (FTO) conductivity was not affected by the high temperature calcination. [25].

The R_{CT} of the studied samples (Fig. S23b) remained constant beyond + 0.5 V vs. RHE. It can be mentioned that the R_{CT} dominates the overall system resistance ($R_{tot} = R_s + R_{CT}$), where $R_{tot} = (dj/dV)\hat{}^{-1}$, reflecting the behavior deduced from the j-V curve. A small fraction of the difference is attributable to a geometric effect, as the double layer capacitance for CN-TiO_2 (Fig. S23c) is higher by a factor of two than the TiO_2 references. The CN-TiO_2 material enjoys a larger effective electrochemical surface area than in the absence of carbon nitride. This effect could be due to an enhanced dispersibility with the Nafion binder enabled by the CN surface: despite the interactions possible between the Nafion's sulfonate groups and the hydroxyls of the TiO_2 surface, the predominantly non-polar, aromatic nature of the polymer gives rise to a better fit with the hydrophobic heptazine units of CN. This leads to augmentation of the catalyst's electrochemical interaction area with the aqueous substrate.

2.10. Structure-activity relationships

The CN(10 %)-TiO_2(90 %) hybrid composite unambiguously merges the properties of its two constituent SCs, resulting in enhanced photoelectroactivity under visible light. Indeed, it displayed a clear superior: benzylamine photooxidation under red light (625 nm), H_2 production under blue light (465 nm), and PEC performance beyond 410 nm. The underlying physico-chemical effects are summarized.

The photosensitization effect was validated through the obtained narrow band gap in the orange CN-TiO_2 composite, measuring 2.9 eV. This outcome is attributed to the new heterointerface (shifting potentials) and vacancies, enhancing the solar spectrum utilization, rapid charge transfer, and prolonged carrier lifetimes.

By integrating steady-state PL, TCSPC, and fs-TAS findings with photoelectrocatalytic measurements, it allows to postulate that the electron transfer occurs from CN to TiO_2 in the hybrid. At an excitation wavelength of 400 nm, a very fast sub-ps charge transfer occurs from the CN to the TiO_2 due to the close interfacial proximity in the solid–solid photoabsorbers contact, thanks to the favorable position of their band edges. Thus, the singlet excited state of the CN in the composite is quenched compared to the CN reference. Unlike CN, which experiences high charge recombination rates, the CN-TiO_2 (10–90 %) heterointerface enhances charge transfer and separation process which in turn increases the catalytic efficiency. At longer wavelengths, beyond 465 nm, proving any charge transfer conclusively is challenging due to weak photoexcitation and limited instrument sensitivity. Conversely, at shorter excitation wavelengths ($\leq$380 nm), the simultaneous excitation of both TiO_2 and CN within the composite makes it difficult to clearly identify charge transfer.

Structural and morphological analysis reinforces the optoelectrical and carrier dynamics findings by confirming the formation of a heterojunction. The inelastic buried electrons indicate a CN overlayer on TiO_2, whilst the presence of abundant C—O deconvoluted signal, compared to CN reference XPS signal, may indicate the interaction at the CN and TiO_2 heterointerface, coexistence of two pores (3.8 and 5.3 nm), and detection of Ti, O, C, and N in EDX and EELS spectra. Furthermore, heptazine fingerprints, a 565 °C decomposition temperature, and a C/N ratio of 0.57 confirm the CN formation thus presence.

Hence, based on both photoelectrocatalysis and characterizations, we observe that CN sensitized TiO_2.

3. Conclusions

In this study, we successfully synthesized a CN(10 %)-TiO_2(90 %) composite using a single solid thermal step, leveraging the synergetic interaction between TiO_2 and CN, resulting in a unique TiO_2 sensitization effect. This new hybrid composite exhibited robust performance in various photo and photoelectrocatalytic reactions, outperforming reference materials and reported catalysts at operational comparable conditions [23,98,99]. The composite exhibited a remarkable four-fold enhancement in benzylamine photooxidation, achieving a 51 % yield at 625 nm (red light), clearly demonstrating the effective TiO_2 sensitization. In photocatalytic hydrogen production, Pt/CN-TiO_2 surpassed the Pt/TiO_2 reference by 1.9-fold and 1.6-fold, yielding notable production rates of 148 and 319 μmol h^{-1} g^{-1} at 465 and 410 nm (blue and violet lights), respectively. Additionally, superior photo(electro)chemistry (PEC) performance was observed, with a 3.4-fold increase and a current density of 62 ± 3 μA cm^{-2} at 0.4 V vs reversible hydrogen electrode (RHE) in triethanolamine (TEOA) solution. CN-TiO_2 also displayed enhanced impedance performance, registering a two-fold increase compared to TiO_2 references, with a value of 10^{-4}F cm^{-2}.

These results underscore our hypothesis that the CN-TiO_2 composite can effectively utilize a broader spectrum of light due to its narrow band gap and efficient charge transfer properties. Innovations in this work include the single-step synthesis method and the demonstrated enhancement in photoelectrocatalytic activity under visible light. Compared to previous literature, our composite shows significant improvements in benzylamine photooxidation and photocatalytic hydrogen production under monochromatic visible light, as well as higher PEC performance and charge transfer efficiency. The CN(10 %)-TiO_2(90 %) composite thus holds great potential as an efficient and versatile photoelectrocatalytic material for solar energy conversion and other critical catalytic applications within a circular economy context, emphasizing the potential for sustainable and green technologies. Although further research is needed to address the technical and economic feasibility of applying CN-TiO_2 on an industrial scale, this work paves the way for future studies to explore potential dopants to improve its efficiency and to scale up the synthesis process for industrial applications.

4. Materials and methods section

4.1. Chemicals

Titanium (IV) oxide, anatase nanopowder, <25 nm particle size, (TiO_2 99.7 % trace metal basis, Sigma Aldrich), melamine ($C_3H_6N_6$), 99 %, Sigma Aldrich), potassium hydroxide (KOH, 99.98 % (metals basis), Alfa Aesar), hexachloroplatinic acid (H_2PtCl_6, 8 wt% in H_2O, Sigma Aldrich), Nafion (15–20 % water, 1100 W, Sigma Aldrich), acetonitrile (CH_3CN, Supelco, hypergrade for LC-MS), ethanol (≥99 %, Sigma Aldrich), methanol (MeOH, ≥99 %, Sigma Aldrich), benzylamine (99 %, Sigma Aldrich), triethanolamine (TEOA, ≥99 %, Sigma Aldrich) were used without further purification.

4.2. Synthesis of TiO_2, CN and TiO_2/CN materials

Two references of TiO_2 anatase were used, one bare without any treatment and a calcined with an applied thermal treatment of 2.3 °C min^{-1} until reaching and staying at 550 °C for 3 h, N_2 1 bar continuous flux. Reference graphitic carbon nitride (CN) was synthesized using melamine under the exact same thermal treatment as that of TiO_2 calcined reference to perform the thermal polycondensation. TiO_2/CN binary composite used melamine as CN precursor and TiO_2 anatase nanoparticles in predetermined mass proportion and followed the same polycondensation protocol as previous CN and TiO_2 references.

4.3. Preparation of electrodes

The working electrode's preparation consists of several steps. First, F-doped tin oxide (FTO) glass is pretreated, through cleaning by sonication in ethanol for 30 min and oven drying at 80 °C. The defined area of 0.25 cm^2 of the FTO glass was protected using Scotch tape. Secondly, 3 mg of each material was weighed in a vial and 20 μL of Nafion (binder) and 0.2 mL of ethanol were added. This slurry was stirred overnight, then sonicated for 15 min and 25 μL of the suspension was deposited by drop casting onto the pretreated FTO coated glass electrode (area 0.25 cm^2). Finally, the electrode was air dried at room temperature for half a day, and the Scotch tape was removed and further dried at 120 °C for 2 h under a continuous flow of Argon to improve adhesion.

4.4. Preparation of thin films

Thin films were prepared for conducting PL and TAS measurements. Transparent thin films' preparation used the four as-prepared samples by mixing 10 mg of each powder in 10 μL of Nafion and 200 μL of ethanol. The slurry was stirred overnight and then sonicated for 30 min before spreading. After sonication, 5 μL of the suspension of TiO_2 references and TiO_2/CN were drop cast onto the FTO in an area of 0.25 cm^2. The same step applies for CN reference, with the slight difference of using 10 μL of its slurry. After ambient drying, these mesoporous films were annealed at 125 °C for 90 min under argon flux.

4.5. Materials characterization

Thermogravimetric analyses (TGA) were performed using a NETZSCH TG 209 F1 device. Each sample was placed into a platinum crucible and heated from room temperature (*ca.* 25 °C) up to 900 °C with a heating rate of 10 °C min^{-1} under a nitrogen flow of 20 mL min^{-1}. The standard deviation of the decomposition temperature of the analyzed samples is ± 10 °C.

Elemental analysis (EA) by combustion was accomplished using a Vario Micro device.

FT-IR ATR spectra were recorded with a Thermo Fisher Nicolet iS5 spectrometer equipped with an attenuated total reflection unit of diamond. Measurements were acquired in the 625–2250 cm^{-1} range with 32 scans and 8 cm^{-1} of resolution.

The diffuse reflectance spectra were obtained using a Shimadzu UV-2600 spectrometer and the apparatus was operated in the approximately range of 200 to 800 nm. The absorbance spectra in the supplementary information were acquired using a PerkinElmer Lambda 950 employing an integrating sphere and a central mount holder. The samples were illuminated by a tungsten halogen lamp in the wavelength range of 200 to 800 nm, controlled with a double grating monochromator and the radiation was detected with a R6872 photomultiplier. The approach to determining the band gap follows the Tauc theory. [64] A Shimadzu UV-3600 spectrometer with an integration sphere attachment was used for transmittance measurements of the samples on FTO.

Steady-state thin film emission spectra were recorded using an Edinburgh Instruments FLS1000 PL spectrometer with excitation and emission double monochromators. This had a PMT – 900 photomultiplier tube detector and a 450 W xenon arc lamp excitation source for acquisition of the steady state spectra. The samples were measured with a front facing illumination scheme. For the acquisition of the emission spectra, all the samples *i.e.*, FTO, TiO_2 550/FTO, CN/FTO and CN-TiO_2/FTO were excited at 320 nm, 380 nm, 400 nm, and 465 nm with slit widths of 1 nm. The 320 and 380 nm wavelengths served to elucidate the charge carrier dynamics in the UV region, while 400 and 465 nm were used to examine carrier dynamics and compare with photoelectrocatalytic visible-light activity.

The Mott-Schottky results were derived from the data analysis of electrochemical impedance spectroscopy, and more details can be found in the respective section below.

The femtosecond transient absorption spectroscopy (fs-TAS) measurements of the samples were acquired using pump–probe spectroscopy. For the pump–probe spectroscopy, the laser pulses at 800 nm were delivered from the Libra F, Coherent Inc., which was coupled with an optical parametric amplifier (OPA) Topas C, Light Conversion Ltd. These laser pulses were utilized to produce the pump (excitation) beam to excite the sample and the probe beam to monitor the spectra. The spectra acquisition at all pump wavelengths were made at the same excitation power (excitation density) of 0.5 ± 0.05 mW (≈0.1 mJ/cm2).

The transient absorption spectra of TiO_2 550/FTO was measured with excitation wavelengths at 320 nm and 380 nm. In addition, CN/FTO and CN-TiO_2/FTO were measured at excitation wavelengths of 320 nm, 380 nm, 400 nm, and 465 nm. The first two wavelengths were used as reference wavelengths to compare the dynamics of all samples and the last two were used to compare the photocatalysis of CN-TiO_2/FTO compared to CN. TiO_2 550/FTO was not included in the measurements at $\geq$ 400 nm excitation because there was no absorption of these samples in the visible range.

For the probe beam, a sapphire crystal was used to produce a continuum of white light in the near-infrared (NIR) and water in the visible range. The central detection wavelength in the NIR and visible ranges were 960 nm, and 600 nm respectively. The probe beam was passed through a delay line with maximum delay time of 5 ns. The transient absorption responses of the probe beam were measured using an ExciPro TA spectrometer (CDP, Inc.). The spectrometer was coupled with an InGaAs diode array to detect NIR wavelengths and a Si charge coupled device (CCD) array to detect visible range wavelengths.

The detailed fitting methodology for the TA data and for the derivation of the DAS spectra is presented in the supporting information under Section S2.

The time-resolved PL decays were measured using a time-correlated single-photon counting (TCSPC) system (PicoQuant, GmBH). This system was equipped with a Picoharp 300 controller and a PDL 800-B driver with the LDH—P—C—405 laser head for excitation at 405 nm (time resolution of 60 ps). The Hamamatsu R2809U microchannel plate photomultiplier was used for signal detection. The fluorescence decays were monitored at 453 nm and 491 nm which corresponds to the emission peak of the singlet excited states in the CN-TiO_2 composite and the CN reference. Information on the fitting of the TCSPC decays is available in the supporting information Section S3.

For scanning transmission electron microscopy (STEM) observations, a suspension of the sample in ethanol was sonicated for 10 min and then drop-casted to an Au grid with a lacey carbon support and dried for 10 min. The STEM study was performed using a double Cs corrected JEOL JEM-ARM200F (S)TEM operated at 80 kV and equipped with a cold-field emission gun. Annular dark-field scanning transmission electron microscopy (ADF − STEM) images were collected at a probe convergence semi-angle of 25 mrad. The solid-state secondary electron detector has been used to record SE-STEM images inside the TEM. EELS spectra were recorded in dual EELs mode at energy dispersions 0.1 eV/ch and 0.25 eV/ch, allowing correction for the zero-loss peak position. The Power law model was used for the background subtraction. Multiple scattering effects have been removed using the Fourier ratio method, implemented in the Gatan Digital micrograph suit.

Wide Angle X-ray Scattering (WAXS) measurements were conducted on the μSpot beamline of BESSY-II (Helmholtz-Zentrum Berlin, HZB, Germany) [100]. Experiments were performed using a monochromatic X-ray beam at 18.0 keV and a beam size of approximately 30 μm width obtained by a sequence of pinholes. The scattered intensities were collected with a Dectris Eiger 9 M detector. Transmission through the sample was calculated from an X-ray fluorescence signal collected from a lead beam stop using RAYSPEC Sirius SD-E65133-BE-INC detector equipped with an 8 μm beryllium window. The primary beam intensity was monitored by using an ion chamber, and recorded values were used to normalize the scattering signal. The sample-to-detector distance of ~ 300 mm allowed for a usable q-range of $\sim 0.06 < q < 43$ nm^{-1}. The scattering q-range was calibrated against silver behenate, and the corresponding measured intensities were normalized against glassy carbon (NIST SRM3600). The resulting data were processed with an in-house developed Python software based on the pyFAI library. [101] Data reduction steps involved integration to 1D scattering curves and subtraction of an instrumental background (*i.e.,* an empty cell or Kapton background). The scattering data were corrected for transmission and primary beam intensity and scaled to absolute intensity units. Crystallite sizes were calculated by Debye-Scherrer equation. [41] The TiO_2 anatase peaks were modelled using Origin 2021 through pseudo-Voigt fitting function. Such function allows to obtain full width half maximum (FWHM) after careful fitting and the FWHM value is used to insert in the crystallite Debye-Scherrer equation (3), where $k_{\alpha1}$ cupper is 1.5402 Å, k1 is the shape factor: 0.94, θ is the XRD pattern position.

$$\tau = \frac{k_{\alpha1}*k1}{FWHM*cos\theta} \tag{3}$$

Nitrogen adsorption/desorption isotherms were performed in a Quantachrome Quadrasorb SI-MP porosimeter at 77.4 K. The samples were degassed prior to the measurements at 150 °C under vacuum (0.5 Torr) for 20 h in a 3P Instruments Masterprep degassing machine. The Brunauer–Emmett–Teller (BET) model was applied to the adsorption isotherm to calculate the specific surface area from the data ($0.05 < P/P0 < 0.2$) using the QuadraWin 5.05. The total pore volume (VT) was calculated from the amount of gas adsorbed at $P/P0 = 0.995$. The pore size distribution was calculated by using a QSDFT model with a slit/cylindrical pore shape using the nitrogen adsorption data.

XPS data was acquired using a Kratos Axis SUPRA using monochromated Al kα (1486.69 eV) X-rays at 15 mA emission and 12 kV HT (180 W) and an analysis area of 700 x 300 μm. The instrument was calibrated to gold metal Au 4f (83.95 eV) and dispersion adjusted give a BE of 932.6 eV for the Cu $2p_{3/2}$ line of metallic copper. Ag $3d_{5/2}$ line FWHM at 10 eV pass energy was 0.54 eV. Source resolution for monochromatic Al Kα X-rays is ~ 0.3 eV. The instrumental resolution was determined to be 0.35 eV at 10 eV pass energy using the Fermi edge of the valence band for metallic silver. Resolution with charge compensation system on determined to be < 1.33 eV FWHM on PTFE. Ce 3d and O 1 s high resolution spectra were obtained individually in binding energy windows of 945 – 870 eV and 540–520 eV respectively using a pass energy of 40 eV, step size of 0.1 eV and dwell time of 100 ms, resulting in a line width of *ca.* 0.7 eV for Au $4f_{7/2}$. Survey spectra were obtained using a pass energy of 160 eV. Charge neutralisation was achieved using an electron flood gun with filament current = 0.4 A, charge balance = 4 V, filament bias = 5 V. Successful neutralisation was adjudged by analysing the C 1 s region wherein a sharp peak with no lower BE structure was obtained. Spectra have been charged corrected to the C 1 s adventitious carbon signal at 284.8 eV. All data was recorded at a base pressure of below 9 x 10^{-9} Torr and a room temperature of 294 K. XPS Data was analysed using CasaXPS v2.3.26rev1.0 N. Peaks were fit with a Shirley background prior to component analysis. Line shapes of LA (1.53, 253) were used for all fitting.

Ti K-edge X-ray absorption spectroscopy (XAS) spectra were collected at the μSpot beamline of the BESSY II synchrotron (Berlin, Germany). [100,102] The X-ray beam delivered by a 7 T wavelength-shifter was focused to a sub-millimeter spot using toroidal mirror and monochromatized using a Si(111) double crystal monochromator. Third order harmonics were rejected by misaligning the monochromator crystals. Samples were placed in a polymethylmethacrylate holder closed with a 25 μm thick polyimide film filter to carry out measurements in transmission mode. Spectra were collected at room temperature using two ionization chambers (FMB Oxford Ltd) to measure the incident and transmitted flux. The energy was calibrated by measuring a 5 nm thick metallic Ti foil simultaneously with every sample. This was achieved by using a third ionization chamber downstream from the sample, so the same X-ray beam was passing through both samples. Extended X-ray absorption fine structure (EXAFS) analysis was carried out by using Demeter software package (ATHENA, ARTEMIS, HEPHAESTUS software's) [103] using standard procedures for background subtraction and Fourier analysis of the oscillations for the determination of the coordination shells.

EPR measurements were conducted on a Bruker EMXnano benchtop X-Band EPR spectrometer. The following settings were used for all spectra acquisition unless other is specified: Center Field 3444.05 G, Sweep Width 200 G, Receiver Gain 60 dB, Modulation Amplitude 1.000 G, Number of Scans 4, Microwave Attenuation 10 dB. Sample was placed and flame-sealed in EPR capillaries (IntraMark, volume 50 μL, ID 0.86 mm), inside EPR tubes (ID 3 mm, OD 4 mm, length 250 mm). *In-situ* EPR measurements of photocatalytic experiments were performed by coupling Thorlabs M415F3 Fiber-Coupled LED (64 mW cm^{-2} measured at 0 cm distance) with Thorlabs DC2200 High-Power LED controller.

Photocatalytic TEMPO Detection Experiment: A solution of 2,2,6,6-tetramethylpiperidine (TEMP) (5 μL, 0.03 mmol) in acetonitrile (CH_3CN) (3 mL) was prepared in a 4 mL glass vial. The solution was flushed via the double needle technique with O_2 for 2 min. The most active catalyst (CN(10 %)-TiO_2(90 %)) was prepared under the same reaction conditions, and it was introduced into a capillary (IntraMark, volume 50 μL, purchased from BRAND GMBH+CO KG) was sealed in the flame of the gas burner from one side. The capillary was charged with an aliquot of the TEMP solution in CH_3CN (20 μL, 0.01 mol L−1). The open end of the capillary was sealed in the flame of a gas burner and placed into an EPR tube (ID 3 mm, OD 4 mm, length 250 mm). The EPR spectrum was acquired and used as a reference (0 min, in dark). Afterward, the sample was directly irradiated using a 415 nm LED module equipped with optic fiber, to perform *in situ* measurements. EPR spectra were acquired immediately when turning the light ON and after 20 min. The acquired spectra were compared with spectra obtained under the same conditions, but using clean uncoated glass capillaries (control experiments). [91].

Photocatalytic DMPO-O_2•– Detection Experiment: A solution of 5,5-Dimethyl-1-pyrroline *N*-oxide (DMPO) (5 μg, 0.04 mmol) in CH_3CN (3 mL) was prepared in a 4 mL glass vial. The solution was flushed via the double needle technique with O_2 for 2 min. The most active catalyst (CN (10 %)-TiO_2(90 %)) was prepared under the same reaction conditions, and it was introduced into a capillary (IntraMark, volume 50 μL, purchased from BRAND GMBH+CO KG) that was sealed in the flame of a gas burner from one side. The capillary was charged with an aliquot of DMPO solution in CH_3CN (20 μL, 0.01 mol L−1). The open end of the capillary was sealed in the flame of a gas burner and placed into an EPR tube (ID 3 mm, OD 4 mm, length 250 mm). The EPR spectrum was acquired and used as a reference (0 min, in dark). Afterward, the sample was directly irradiated using a 415 nm LED module equipped with optic fiber, to perform *in situ* measurements. EPR spectra were acquired immediately after turning the light source ON and after 20 min. The acquired spectra were compared with the spectra obtained under the same conditions, but using clean uncoated glass capillaries (control experiments). [91].

Irradiance of the LED modules was measured using PM400 Optical Power and Energy Meter equipped with the integrating sphere S142C and purchased from Thorlabs.

The reported errors include the precision of each measuring instrument, and, in some cases, the variability observed in triplicate measurements.

4.6. Performance tests

4.6.1. Photooxidation of benzylamine

In a vial of 4 mL, 5 mg of catalyst are weighted, 5 μL of benzylamine and 1 mL of acetonitrile are added. The vial is saturated with O_2 atmosphere for 2 min. The vial is stirred at 800 rpm and exposed to a monochromatic LED red lamp light (625 nm, 50 W) for 72 h. After the reaction, a few μL are taken to fill the third part of a gas chromatography (GC) vial and completed with acetonitrile to quantify the resulting conversion to dibenzylimine via GC. The unconverted benzylamine is also quantified for internal control, both against a calibration curve using a standard dibenzylimine solution.

4.6.2. Photocatalytic tests for H_2 production

Photocatalytic H_2 evolution activities were evaluated in a closed system equipped with a pressure detector to examine the pressure of the evolved gases in during photocatalytic reactions. Purple LED (50 W, $\lambda = 410$ nm) and blue LED (50 W, $\lambda = 465$ nm) was used for photocatalytic H_2 evolution evaluation, respectively. The used volume of the reactor was 38 mL, and the temperature was controlled 298 K by cycle water. Theevolved amounts of the gases were finally calculated by the Clausius–Clapeyron relation (PV=nRT). Typically, 50 mg of solid catalysts was dispersed into 38 mL of DI water and TEOA (10 vol%) mixture,while they were degassed in advance for use with vacuum and sonication, respectively. 3 wt% of Pt cocatalyst were deposited by a typical *in-situ* photo deposition strategy fromH_2PtCl_6 precursor. The H_2 evolution rate was calculated excluding the first reaction hour.

The AQY Measurement and Wavelength Experiment.

H_2 evolution AQY was measured using a monochromatic visible light (420 ± 1.0 nm). The AQY was calculated as follows:

$$AQY(\%) = \frac{2xr_{H2}xN_Axhc}{SxIx\lambda}$$

where r_{H2} is the production rate of H_2 molecules (mol s^{-1}), NA is Avogadro constant (6.022×10^{23} mol^{-1}),hc is the Planck constant (6.626×10^{-34} J s^{-1}) multiplied by c the speed of light (3×10^8 m s^{-1}) giving ($1.98644586 \times 10^{-25}$ J m), S is the irradiation area (cm^2), I is the intensity of irradiation light (W cm^{-2}), andλ is the wavelength of the monochromatic light (m).

4.6.3. Electrochemical characterization

The electrochemical measurements of oxygen evolution were performed in a IviumStat potentiostat using a 3-electrode cell. Such a cell consists of a Pt wire as a counter electrode, Ag/AgCl as a reference electrode, and FTO glass coated with the material as a working electrode. An aqueous solution of KOH (0.1 M) was used as an electrolyte and all the measurements were done at ambient temperature. The cyclic/linear sweep voltammetry (CV/LSV). LSV and CV curves were acquired at 10 and 20 mV s^{-1} of scan rate, respectively. The electrode potentials in all curves were converted to the reversible hydrogen electrode (RHE) scale using the following equation: E(NHE) = E(Ag/AgCl) + 0.197 + 0.059 × pH V.

4.6.4. Photoelectrochemical test

For photoelectrochemical measurements, the same electrochemical (3 electrodes) cell using a 150 W xenon arc lamp (LOT-Quantum Design GmbH, LSE140/160.25C), that was calibrated to AM 1.5G, was used as the light source.

4.6.5. Electrochemical impedance spectroscopy (EIS)

EIS measurements were performed using the same 3 electrode cell as for the electrochemical characterization experiments. The EIS samples measurements were acquired in the potential range from − 2 to 1.2 V RHE, 0.05 V potential step, and frequencies from 10 kHz to 100 mHz, 10 mV potential amplitude. Nyquist plots were obtained by measuring the

EIS. Z-View software was used to extract resistances and capacitance from the Nyquist plots by fitting the experimental data to a simple Randles' equivalent circuit.

CRediT authorship contribution statement

Ingrid F. Silva: Writing – review & editing, Investigation, Formal analysis, Data curation. **Carolina Pulignani:** Writing – review & editing, Investigation, Formal analysis, Data curation. **Jokotadeola Odutola:** Writing – review & editing, Investigation, Formal analysis, Data curation. **Alexey Galushchinskiy:** Investigation, Formal analysis. **Ivo F. Teixeira:** Writing – review & editing, Investigation, Formal analysis, Data curation. **Mark Isaacs:** Writing – review & editing, Visualization, Validation, Investigation, Formal analysis, Data curation. **Camilo A. Mesa:** Writing – review & editing, Validation, Investigation, Formal analysis, Data curation. **Ernesto Scoppola:** Writing – review & editing, Validation, Investigation, Formal analysis, Data curation. **Albert These:** Investigation, Formal analysis, Data curation. **Bolortuya Badamdorj:** Investigation, Formal analysis, Data curation. **Miguel Ángel Muñoz-Márquez:** Writing – review & editing, Formal analysis, Data curation. **Ivo Zizak:** Writing – review & editing, Investigation, Formal analysis, Data curation. **Robert Palgrave:** Investigation, Formal analysis. **Nadezda V. Tarakina:** Writing – review & editing, Investigation, Formal analysis, Data curation. **Sixto Gimenez:** Writing – review & editing, Investigation, Formal analysis. **Christoph Brabec:** Writing – review & editing, Investigation. **Julien Bachmann:** Writing – review & editing, Investigation, Formal analysis. **Emiliano Cortes:** Writing – review & editing, Investigation. **Nikolai Tkachenko:** Writing – review & editing, Investigation, Formal analysis, Data curation. **Oleksandr Savateev:** Writing – review & editing, Investigation, Formal analysis, Data curation. **Pablo Jiménez-Calvo:** Writing – review & editing, Writing – original draft, Validation, Supervision, Software, Resources, Project administration, Methodology, Investigation, Formal analysis, Data curation, Conceptualization.

Declaration of competing interest

The authors declare that they have no known competing financial interests or personal relationships that could have appeared to influence the work reported in this paper.

Data availability

No data was used for the research described in the article.

Acknowledgements

The authors thank the Max Planck Society for its financial support. I. F.S thanks the Alexander von Humbolt Foundation for her postdoctoral fellowship. P.J-C has received funding from the European Union's Horizon Europe research and innovation programme under the Marie Skłodowska-Curie grant agreement N° 101068996. C.A.M. acknowledges funding from UJI postdoc fellowship POSDOC/2019/20, the Generalitat Valenciana for the APOSTD/2021/251 fellowship. This project has received funding from the European Union's Horizon 2020 research and innovation program under the Marie Skłodowska-Curie grant agreement N° 861151 Solar2Chem. P.J-C acknowledges Prof. Antonietti for his scientific and management support. The X-ray photoelectron (XPS) data collection was performed at the EPSRC National Facility for XPS ("HarwellXPS"), operated by Cardiff University and UCL, under Contract No. PR16195. We are thankful to Dr. Chenghao Li for the assistance with data reduction tools such as DPDAK and for the user support during the WAXS and XAS experiments on the μSpot beamline. Access to the beamline was granted by the Biomaterial Department of the Max Planck Institute of Colloids and Interfaces and Helmholtz Zentrum Berlin. We thank Dr. Wolfgang Wagermaier for fruitful discussions for designing and performing experiments on the μSpot beamline of BESSY II synchrotron. We thank Prof. Reisner for the scientific discussions. I.F.T. acknowledges the Brazilian funding agencies CNPq (423196/2018-9, 403064/2021-0 and 405752/2022-9) and FAPESP (2020/14741-6, 2021/13271-9 and 2021/12394-0). S.G. acknowledges support from the project PID2020-116093RB-C41 funded by MCIN/AEI/10.13039/501100011033/. We dedicate this work to the memory of Prof. Nikolai Tkachenko, whose contributions and dedication were invaluable to this research.

Open access funding enabled and organized by Projekt DEAL.

Appendix A. Supplementary data

Supplementary data to this article can be found online at https://doi.org/10.1016/j.jcis.2024.09.028.

References

[1] K. Sivula, R. van de Krol, Semiconducting materials for photoelectrochemical energy conversion, Nat. Rev. Mater. 1 (2016) 15010, https://doi.org/10.1038/natrevmats.2015.10.

[2] A. Fujishima, K. Honda, Electrochemical photolysis of water at a semiconductor electrode, Nature 238 (1972) 37–38, https://doi.org/10.1038/238037a0.

[3] K. Takanabe, Photocatalytic Water Splitting: Quantitative Approaches toward Photocatalyst by Design, ACS Catal. 7 (2017) 8006–8022, https://doi.org/10.1021/acscatal.7b02662.

[4] A. Kudo, Y. Miseki, Heterogeneous photocatalyst materials for water splitting, Chem. Soc. Rev. 38 (2009) 253–278, https://doi.org/10.1039/b800489g.

[5] U. Caudillo-Flores, M.J. Muñoz-Batista, M. Fernández-García, A. Kubacka, Bimetallic Pt-Pd co-catalyst Nb-doped TiO2 materials for H2 photo-production under UV and Visible light illumination, Appl. Catal. B Environ. 238 (2018) 533–545, https://doi.org/10.1016/J.APCATB.2018.07.047.

[6] J. Xing, J.F. Chen, Y.H. Li, W.T. Yuan, Y. Zhou, L.R. Zheng, H.F. Wang, P. Hu, Y. Wang, H.J. Zhao, et al., Stable Isolated Metal Atoms as Active Sites for Photocatalytic Hydrogen Evolution, Chem. - A Eur. J. 20 (2014) 2138–2144, https://doi.org/10.1002/chem.201303366.

[7] J.A. Diaz-Real, P. Elsaesser, T. Holm, W. Mérida, Electrochemical reduction on nanostructured TiO2 for enhanced photoelectrocatalytic oxidation, Electrochim. Acta 329 (2020) 135162, https://doi.org/10.1016/j.electacta.2019.135162.

[8] M. Bingham, A. Mills, Photonic efficiency and selectivity study of M (M=Pt, Pd, Au and Ag)/TiO2 photocatalysts for methanol reforming in the gas phase, J. Photochem. Photobiol. A Chem. 389 (2020) 112257, https://doi.org/10.1016/J.JPHOTOCHEM.2019.112257.

[9] P. Jimenéz-Calvo, M.J. Muñoz-Batista, M. Isaacs, V. Ramnarain, D. Ihiawakrim, X. Li, M. Ángel Muñoz-Márquez, G. Teobaldi, M. Kociak, E. Paineau, A compact photoreactor for automated H2 photoproduction: Revisiting the (Pd, Pt, Au)/TiO2 (P25) Schottky junctions, Chem. Eng. J. 459 (2023) 141514, https://doi.org/10.1016/J.CEJ.2023.141514.

[10] T. Dittrich, J. Sydorenko, N. Spalatu, N.H. Nickel, A. Mere, M. Krunks, I. Oja Acik, Synthesis Control of Charge Separation at Anatase TiO2Thin Films Studied by Transient Surface Photovoltage Spectroscopy, ACS Appl. Mater. Interfaces 14 (2022) 43163–43170, https://doi.org/10.1021/ACSAMI.2C09032/ASSET/IMAGES/LARGE/AM2C09032_0007.JPEG.

[11] Z. Wei, M. Janczarek, M. Endo, K. Wang, A. Balčytis, A. Nitta, M.G. Méndez-Medrano, C. Colbeau-Justin, S. Juodkazis, B. Ohtani, et al., Noble Metal-Modified Faceted Anatase Titania Photocatalysts: Octahedron versus Decahedron, Appl. Catal. B Environ. (2018), https://doi.org/10.1016/j.apcatb.2018.06.027.

[12] M.K. Nazeeruddin, E. Baranoff, M. Grätzel, Dye-sensitized solar cells: A brief overview, Sol. Energy 85 (2011) 1172–1178, https://doi.org/10.1016/j.solener.2011.01.018.

[13] Z.H.N. Al-Azri, W.-T. Chen, A. Chan, V. Jovic, T. Ina, H. Idriss, G.I.N. Waterhouse, The roles of metal co-catalysts and reaction media in photocatalytic hydrogen production: Performance evaluation of M/TiO_2 photocatalysts (M = Pd, Pt, Au) in different alcohol–water mixtures, J. Catal. 329 (2015) 355–367, https://doi.org/10.1016/J.JCAT.2015.06.005.

[14] J. Low, J. Yu, M. Jaroniec, S. Wageh, A.A. Al-Ghamdi, Heterojunction Photocatalysts at Wiley-VCH Verlag (2017), https://doi.org/10.1002/adma.201601694.

[15] Wang, Y., Vogel, A., Sachs, M., Sebastian Sprick, R., Wilbraham, L., A Moniz, S.J., Godin, R., Zwijnenburg, M.A., Durrant, J.R., Cooper, A.I., et al. (2019). Current understanding and challenges of solar-driven hydrogen generation using polymeric photocatalysts. Nat. Energy *4*, 746–760. 10.1038/s41560-019-0456-5.

[16] P. Jiménez-Calvo, V. Caps, V. Keller, Plasmonic Au-based junctions onto TiO2, gC3N4, and TiO2-gC3N4 systems for photocatalytic hydrogen production: Fundamentals and challenges, Renew. Sustain. Energy Rev. 149 (2021) 111095, https://doi.org/10.1016/J.RSER.2021.111095.

[17] Serpone, N., and Emeline, A. V. (2012). Semiconductor photocatalysis - Past, present, and future outlook at American Chemical Society, 10.1021/jz300071j 10.1021/jz300071j.

[18] J. Qin, J. Barrio, G. Peng, J. Tzadikov, L. Abisdris, M. Volokh, M. Shalom, Direct growth of uniform carbon nitride layers with extended optical absorption towards

efficient water-splitting photoanodes, Nat. Commun. 11 (2020) 4701, https://doi.org/10.1038/s41467-020-18535-0.

[19] M. Grätzel, Dye-sensitized solar cells, J Photochem Photobiol c: Photochem Rev 4 (2003) 145–153, https://doi.org/10.1016/S1389-5567(03)00026-1.

[20] B. O'Regan, M. Grätzel, A low-cost, high-efficiency solar cell based on dye-sensitized colloidal TiO_2 films, Nature 353 (1991) 737–740, https://doi.org/10.1038/353737a0.

[21] A. Listorti, B. O'Regan, J.R. Durrant, Electron transfer dynamics in dye-sensitized solar cells, Chem. Mater. 23 (2011) 3381–3399, https://doi.org/10.1021/CM200651E/ASSET/IMAGES/MEDIUM/CM-2011-00651E_0010.GIF.

[22] C.A. Caputo, L. Wang, R. Beranek, E. Reisner, Carbon nitride–TiO_2 hybrid modified with hydrogenase for visible light driven hydrogen production, Chem. Sci. 6 (2015) 5690–5694, https://doi.org/10.1039/C5SC02017D.

[23] P. Jiménez-Calvo, V. Caps, M.N. Ghazzal, C. Colbeau-Justin, V. Keller, Au/TiO_2(P25)-gC_3N_4 composites with low gC_3N_4 content enhance TiO_2 sensitization for remarkable H_2 production from water under visible-light irradiation, Nano Energy 75 (2020) 104888, https://doi.org/10.1016/j.nanoen.2020.104888.

[24] L. Zhou, L. Wang, J. Zhang, J. Lei, Y. Liu, The preparation, and applications of g-C_3N_4/TiO_2 heterojunction catalysts—a review at Springer, Netherlands (2017), https://doi.org/10.1007/s11164-016-2748-8.

[25] C. Pulignani, C.A. Mesa, S.A.J. Hillman, T. Uekert, S. Giménez, J.R. Durrant, E. Reisner, Rational Design of Carbon Nitride Photoelectrodes with High Activity Toward Organic Oxidations, Angew. Chemie Int. Ed. 61 (2022) e202211587.

[26] C. Miranda, H. Mansilla, J. Yáñez, S. Obregón, G. Colón, Improved photocatalytic activity of g-C3N4/TiO2 composites prepared by a simple impregnation method, J. Photochem. Photobiol. A Chem. 253 (2013) 16–21, https://doi.org/10.1016/j.jphotochem.2012.12.014.

[27] C. Wang, Y. Zhao, H. Xu, Y. Li, Y. Wei, J. Liu, Z. Zhao, Efficient Z-scheme photocatalysts of ultrathin g-C3N4-wrapped Au/TiO2-nanocrystals for enhanced visible-light-driven conversion of CO2 with H2O, Appl. Catal. B Environ. 263 (2020) 118314, https://doi.org/10.1016/j.apcatb.2019.118314.

[28] X. Wei, C. Shao, X. Li, N. Lu, K. Wang, Z. Zhang, Y. Liu, Facile in situ synthesis of plasmonic nanoparticles-decorated g-$C_{3}N_{4}$/TiO_{2} heterojunction nanofibers and comparison study of their photosynergistic effects for efficient photocatalytic H_2 evolution, Nanoscale 8 (2016) 11034–11043, https://doi.org/10.1039/C6NR01491G.

[29] J. Wang, J. Ma, Q. Zhang, Y. Chen, L. Hong, B. Wang, J. Chen, H. Jing, New heterojunctions of CN/TiO2 with different band structure as highly efficient catalysts for artificial photosynthesis, Appl. Catal. B Environ. 285 (2021) 119781, https://doi.org/10.1016/j.apcatb.2020.119781.

[30] J. Barrio, D. Mateo, J. Albero, H. García, M. Shalom, A Heterogeneous Carbon Nitride-Nickel Photocatalyst for Efficient Low-Temperature CO_2 Methanation, Adv. Energy Mater. 9 (2019), https://doi.org/10.1002/aenm.201902738.

[31] M. Bledowski, L. Wang, A. Ramakrishnan, O.V. Khavryuchenko, V. D. Khavryuchenko, P.C. Ricci, J. Strunk, T. Cremer, C. Kolbeck, R. Beranek, Visible-light photocurrent response of TiO_2 –polyheptazine hybrids: evidence for interfacial charge-transfer absorption, PCCP 13 (2011) 21511–21519, https://doi.org/10.1039/C1CP22861G.

[32] R. Gong, D. Mitoraj, D. Gao, M. Mundszinger, D. Sorsche, U. Kaiser, C. Streb, R. Beranek, S. Rau, A Triad Photoanode for Visible Light-Driven Water Oxidation via Immobilization of Molecular Polyoxometalate on Polymeric Carbon Nitride, Adv. Sustain. Syst. 6 (2022), https://doi.org/10.1002/adsu.202100473.

[33] P. Jiménez-Calvo, Synergy of visible-light responsive photocatalytic materials and device engineering for energy and environment: Minireview on hydrogen production and water decontamination, Mater. Today Catal. 4 (2024) 100040, https://doi.org/10.1016/J.MTCATA.2024.100040.

[34] Maier, S.A. (2007). Plasmonics : fundamentals and applications (Springer).

[35] G. Sportelli, M. Marchi, P. Fornasiero, G. Filippini, F. Franco, M. Melchionna, G. Sportelli, M. Marchi, P. Fornasiero, G. Filippini, et al., Photoelectrocatalysis for Hydrogen Evolution Ventures into the World of Organic Synthesis, Glob. Challenges 2400012 (2024), https://doi.org/10.1002/GCH2.202400012.

[36] J. Garcia-Navarro, M.A. Isaacs, M. Favaro, D. Ren, W.-J. Ong, M. Grätzel, P. Jiménez-Calvo, Updates on Hydrogen Value Chain: A Strategic Roadmap, Glob. Challenges 2300073 (2023), https://doi.org/10.1002/GCH2.202300073.

[37] X. Chen, C. Li, M. Grätzel, R. Kostecki, S.S. Mao, Nanomaterials for renewable energy production and storage, Chem. Soc. Rev. 41 (2012) 7909, https://doi.org/10.1039/c2cs35230c.

[38] Diab, G.A.A., da Silva, M.A.R., Rocha, G.F.S.R., Noleto, L.F.G., Rogolino, A., de Mesquita, J.P., Jiménez-Calvo, P., and Teixeira, I.F. (2023). A Solar to Chemical Strategy: Green Hydrogen as a Means, Not an End. Glob. Challenges. 10.1002/gch2.202300185.

[39] Y. Pellegrin, F. Odobel, Sacrificial electron donor reagents for solar fuel production, Comptes Rendus Chim. 20 (2017) 283–295, https://doi.org/10.1016/j.crci.2015.11.026.

[40] J. Fu, J. Yu, C. Jiang, B. Cheng, g-C3N4-Based Heterostructured Photocatalysts, Adv. Energy Mater. 8 (2018) 1701503, https://doi.org/10.1002/AENM.201701503.

[41] M. Jerigova, Y. Markushyna, I.F. Teixeira, B. Badamdorj, M. Isaacs, D. Cruz, I. Lauermann, M.Á. Muñoz-Márquez, N.V. Tarakina, N. López-Salas, et al., Green Light Photoelectrocatalysis with Sulfur-Doped Carbon Nitride: Using Triazole-Purpald for Enhanced Benzylamine Oxidation and Oxygen Evolution Reactions, Adv. Sci. 2300099 (2023), https://doi.org/10.1002/ADVS.202300099.

[42] H. Shi, S. Long, S. Hu, J. Hou, W. Ni, C. Song, K. Li, G.G. Gurzadyan, X. Guo, Interfacial charge transfer in 0D/2D defect-rich heterostructures for efficient solar-driven CO2 reduction, Appl. Catal. B Environ. 245 (2019) 760–769, https://doi.org/10.1016/J.APCATB.2019.01.036.

[43] O. Elbanna, M. Fujitsuka, T. Majima, g-C3N4/TiO2 Mesocrystals Composite for H2 Evolution under Visible-Light Irradiation and Its Charge Carrier Dynamics, ACS Appl. Mater. Interfaces 9 (2017) 34844–34854, https://doi.org/10.1021/acsami.7b08548.

[44] Y. Markushyna, C.A. Smith, A. Savateev, Organic Photocatalysis: Carbon Nitride Semiconductors vs, Molecular Catalysts. European J. Org. Chem. 2020 (2020) 1294–1309, https://doi.org/10.1002/ejoc.201901112.

[45] Complexity, T.O. of E. Imines, derivatives, salts thereof. https://oec.world/en/profile/hs/imines-derivatives-salts-thereof.

[46] A.J. Bard, Photoelectrochemistry and heterogeneous photocatalysis at semiconductors, J. Photochem. 10 (1979) 59–75, https://doi.org/10.1016/0047-2670(79)80037-4.

[47] N. Karjule, R.S. Phatake, S. Barzilai, B. Mondal, A. Azoulay, A.I. Shames, M. Volokh, J. Albero, H. García, M. Shalom, Photoelectrochemical alcohols oxidation over polymeric carbon nitride photoanodes with simultaneous H_2 production, J. Mater. Chem. A 10 (2022) 16585–16594, https://doi.org/10.1039/D2TA03660F.

[48] N. Karjule, C. Singh, J. Barrio, J. Tzadikov, I. Liberman, M. Volokh, E. Palomares, I. Hod, M. Shalom, N. Karjule, et al., Carbon Nitride-Based Photoanode with Enhanced Photostability and Water Oxidation Kinetics, Adv. Funct. Mater. 31 (2021) 2101724, https://doi.org/10.1002/ADFM.202101724.

[49] T. Reier, D. Teschner, T. Lunkenbein, A. Bergmann, S. Selve, R. Kraehnert, R. Schlögl, P. Strasser, Electrocatalytic Oxygen Evolution on Iridium Oxide: Uncovering Catalyst-Substrate Interactions and Active Iridium Oxide Species, J. Electrochem. Soc. 161 (2014) F876–F882, https://doi.org/10.1149/2.0411409JES/XML.

[50] S. Chen, H. Huang, P. Jiang, K. Yang, J. Diao, S. Gong, S. Liu, M. Huang, H. Wang, Q. Chen, Mn-Doped RuO2 Nanocrystals as Highly Active Electrocatalysts for Enhanced Oxygen Evolution in Acidic Media, ACS Catal. 10 (2020) 1152–1160, https://doi.org/10.1021/ACSCATAL.9B04922/SUPPL_FILE/CS9B04922_SI_001.PDF.

[51] M. Grätzel, Photoelectrochemical cells, Nature 414 (2001) 338–344, https://doi.org/10.1038/35104607.

[52] M. Isaacs, J. Garcia-Navarro, W.-J. Ong, P. Jiménez-Calvo, Is Photocatalysis the Next Technology to Produce Green Hydrogen to Enable the Net Zero Emissions Goal? Glob. Challenges 2200165 (2022) https://doi.org/10.1002/GCH2.202200165.

[53] Paineau, E., Teobaldi, G., and Jiménez-Calvo, P. (2023). Imogolite Nanotubes and Their Permanently Polarized Bifunctional Surfaces for Photocatalytic Hydrogen Production. Glob. Challenges. 10.1002/gch2.202300255.

[54] Takata, T., Jiang, J., Sakata, Y., Nakabayashi, M., Shibata, N., Nandal, V., Seki, K., Hisatomi, T., and Domen, K. (2020). Photocatalytic water splitting with a quantum efficiency of almost unity. Nat. 2020 5817809 *581*, 411–414. 10.1038/s41586-020-2278-9.

[55] P. Jimenéz-Calvo, Y. Naciri, A. Sobolewska, M. Isaacs, Y. Zhang, A. Leforestier, J. Degrouard, S. Rouzière, C. Goldmann, D. Vantelon, et al., Ti-Modified Imogolite Nanotubes as Promising Photocatalyst 1D Nanostructures for H_2 Production, Small Methods (2023), https://doi.org/10.1002/smtd.202301369.

[56] A. Savateev, D. Dontsova, B. Kurpil, M. Antonietti, Highly crystalline poly (heptazine imides) by mechanochemical synthesis for photooxidation of various organic substrates using an intriguing electron acceptor – Elemental sulfur, J. Catal. 350 (2017) 203–211, https://doi.org/10.1016/j.jcat.2017.02.029.

[57] Hazra, S., Malik, E., Nair, A., Tiwari, V., Dolui, P., and Elias, A.J. (2020). Catalytic Oxidation of Alcohols and Amines to Value-Added Chemicals using Water as the Solvent. Chem. – An Asian J. *15*, 1916–1936. 10.1002/asia.202000299.

[58] B. Jürgens, E. Irran, J. Senker, P. Kroll, H. Müller, W. Schnick, Melem (2,5,8-Triamino-tri- s -triazine), an Important Intermediate during Condensation of Melamine Rings to Graphitic Carbon Nitride: Synthesis, Structure Determination by X-ray Powder Diffractometry, Solid-State NMR, and Theoretical Studies, J. Am. Chem. Soc. 125 (2003) 10288–10300, https://doi.org/10.1021/ja0357689.

[59] I.F. Silva, R.D.F. Rios, O. Savateev, I.F. Teixeira, Carbon Nitride-Based Nanomaterials as a Sustainable Catalyst for Biodiesel Production, ACS Appl. Nano Mater. 6 (2023) 9718–9727, https://doi.org/10.1021/ACSANM.3C01424.

[60] P. Jiménez-Calvo, C. Marchal, T. Cottineau, V. Caps, V. Keller, Influence of the gas atmosphere during the synthesis of g-C3N4 for enhanced photocatalytic H2 production from water on Au/g-C3N4 composites, J. Mater. Chem. A 7 (2019) 14849–14863, https://doi.org/10.1039/c9ta01734h.

[61] Silva, I.F., Teixeira, I.F., Rios, R.D.F., do Nascimento, G.M., Binatti, I., Victória, H. F.V., Krambrock, K., Cury, L.A., Teixeira, A.P.C., and Stumpf, H.O. (2021). Amoxicillin photodegradation under visible light catalyzed by metal-free carbon nitride: An investigation of the influence of the structural defects. J. Hazard. Mater. *401*, 123713. 10.1016/J.JHAZMAT.2020.123713.

[62] Miklavcic, S.J., and Yang, L. (2005). Revised Kubelka–Munk theory. III. A general theory of light propagation in scattering and absorptive media. JOSA A, Vol. 22, Issue 9, pp. 1866-1873 *22*, 1866–1873. 10.1364/JOSAA.22.001866.

[63] H. Tang, K. Prasad, R. Sanjinès, P.E. Schmid, F. Lévy, Electrical and optical properties of TiO2 anatase thin films, J. Appl. Phys. 75 (1994) 2042–2047, https://doi.org/10.1063/1.356306.

[64] J. Tauc, R. Grigorovici, A. Vancu, Optical Properties and Electronic Structure of Amorphous Germanium, Phys. Status Solidi 15 (1966) 627–637, https://doi.org/10.1002/PSSB.19660150224.

[65] H. Yan, H. Yang, TiO2–g-C3N4 composite materials for photocatalytic H2 evolution under visible light irradiation, J. Alloy. Compd. 509 (2011) L26–L29, https://doi.org/10.1016/J.JALLCOM.2010.09.201.

[66] H. Habuchi, H. Koketsu, T. Katsuno, Optical properties of amorphous carbon nitride films with high nitrogen content, Diam. Relat. Mater. 16 (2007) 1340–1342, https://doi.org/10.1016/J.DIAMOND.2007.01.028.

[67] Jiménez-Calvo, P.I. (2019). Synthesis, characterization, and performance of g-C3N4 based materials decorated with Au nanoparticles for (photo) catalytic applications.

[68] I.F. Teixeira, P. Jiménez-Calvo, Carbon nitrides and titanium dioxide-based photocatalysis outlook and challenges: an overview of hydrogen production, transport, storage, safety, and principles, in: Renewable Energy Production and Distribution, Volume 2, (Academic Press), 2023, pp. 145–180, https://doi.org/10.1016/B978-0-443-18439-0.00004-5.

[69] Valery N. Khabashesku, John L. Zimmerman, A., and Margrave, J.L. (2000). Powder Synthesis and Characterization of Amorphous Carbon Nitride. Chem. Mater. *12*, 3264–3270. 10.1021/CM000328R.

[70] Zhang, Y., Pan, Q., Chai, G., Liang, M., Dong, G., Zhang, Q., and Qiu, J. (2013). Synthesis and luminescence mechanism of multicolor-emitting g-C3N4 nanopowders by low temperature thermal condensation of melamine. Sci. Reports 2013 31 *3*, 1–8. 10.1038/srep01943.

[71] J. Wang, J. Huang, H. Xie, A. Qu, Synthesis of g-C3N4/TiO2 with enhanced photocatalytic activity for H2 evolution by a simple method, Int. J. Hydrogen Energy 39 (2014) 6354–6363, https://doi.org/10.1016/J.IJHYDENE.2014.02.020.

[72] R. Godin, Y. Wang, M.A. Zwijnenburg, J. Tang, J.R. Durrant, Time-Resolved Spectroscopic Investigation of Charge Trapping in Carbon Nitrides Photocatalysts for Hydrogen Generation, J. Am. Chem. Soc. 139 (2017) 5216–5224, https://doi.org/10.1021/JACS.7B01547/ASSET/IMAGES/LARGE/JA-2017-01547K_0010.JPEG.

[73] A. Savateev, S. Pronkin, J.D. Epping, M.G. Willinger, C. Wolff, D. Neher, M. Antonietti, D. Dontsova, Potassium Poly(heptazine imides) from Aminotetrazoles: Shifting Band Gaps of Carbon Nitride-like Materials for More Efficient Solar Hydrogen and Oxygen Evolution, ChemCatChem 9 (2017) 167–174, https://doi.org/10.1002/CCTC.201601165.

[74] R. Hao, G. Wang, H. Tang, L. Sun, C. Xu, D. Han, Template-free preparation of macro/mesoporous g-C3N4/TiO2 heterojunction photocatalysts with enhanced visible light photocatalytic activity, Appl. Catal. B Environ. 187 (2016) 47–58, https://doi.org/10.1016/J.APCATB.2016.01.026.

[75] Z. Chen, A. Savateev, S. Pronkin, V. Papaefthimiou, C. Wolff, M. Georg Willinger, E. Willinger, D. Neher, M. Antonietti, D. Dontsova, et al., "The Easier the Better" Preparation of Efficient Photocatalysts—Metastable Poly(heptazine imide) Salts, Adv. Mater. 29 (2017) 1700555, https://doi.org/10.1002/ADMA.201700555.

[76] R. Berera, R. van Grondelle, J.T.M. Kennis, Ultrafast transient absorption spectroscopy: Principles and application to photosynthetic systems, Photosynth. Res. 101 (2009) 105–118, https://doi.org/10.1007/S11120-009-9454-Y/FIGURES/5.

[77] H.P. Pasanen, R. Khan, J.A. Odutola, N.V. Tkachenko, Transient Absorption Spectroscopy of Films: Impact of Refractive Index, J. Phys. Chem. C 128 (2024) 6179, https://doi.org/10.1021/ACS.JPCC.4C00981/ASSET/IMAGES/LARGE/JP4C00981_0004.JPEG.

[78] I.F. Teixeira, N.V. Tarakina, I.F. Silva, N. López-Salas, A. Savateev, M. Antonietti, Overcoming Electron Transfer Efficiency Bottlenecks for Hydrogen Production in Highly Crystalline Carbon Nitride-Based Materials, Adv. Sustain. Syst. 2100429 (2022), https://doi.org/10.1002/ADSU.202100429.

[79] C.F. Holder, R.E. Schaak, Tutorial on Powder X-ray Diffraction for Characterizing Nanoscale Materials, ACS Nano 13 (2019) 7359–7365, https://doi.org/10.1021/ACSNANO.9B05157/ASSET/IMAGES/MEDIUM/NN-2019-051577_0009.GIF.

[80] L.-Q. Weng, S.-H. Song, S. Hodgson, A. Baker, J. Yu, Synthesis and characterisation of nanotubular titanates and titania, J. Eur. Ceram. Soc. 26 (2006) 1405–1409, https://doi.org/10.1016/J.JEURCERAMSOC.2005.01.058.

[81] P. Jiménez-Calvo, L. Michel, V. Keller, V. Caps, Titania-Carbon Nitride Interfaces in Gold-Catalyzed CO Oxidation, ACS Appl. Mater. Interfaces 13 (2021) 61015–61026, https://doi.org/10.1021/ACSAMI.1C16159/SUPPL_FILE/AM1C16159_SI_001.PDF.

[82] S. Brunauer, P.H. Emmett, E. Teller, Adsorption of Gases in Multimolecular Layers, J. Am. Chem. Soc. 60 (1938) 309–319, https://doi.org/10.1021/ja01269a023.

[83] C.-K. Lee, C.-C. Wang, M.-D. Lyu, L.-C. Juang, S.-S. Liu, S.-H. Hung, Effects of sodium content and calcination temperature on the morphology, structure and photocatalytic activity of nanotubular titanates, J. Colloid Interface Sci. 316 (2007) 562–569, https://doi.org/10.1016/J.JCIS.2007.08.008.

[84] H. Wang, P. Jiménez-Calvo, M. Hepp, M. Isaacs, C. Otieno Ogolla, I. Below-Lutz, B. Butz, V. Strauss, Laser-Patterned Porous Carbon/ZnO Nanostructure Composites for Selective Room Temperature Sensing of Volatile Organic Compounds, ACS Appl, Nano Mater, 2022.

[85] S. Tougaard, QUASES-IMFP-TPP2M program, Quases-Tougaard Inc., 2002.

[86] D.O. Scanlon, C.W. Dunnill, J. Buckeridge, S.A. Shevlin, A.J. Logsdail, S. M. Woodley, C.R.A. Catlow, M.J. Powell, R.G. Palgrave, I.P. Parkin, et al., Band alignment of rutile and anatase TiO_2, Nat. Mater. 12 (2013) 798–801, https://doi.org/10.1038/nmat3697.

[87] B. Coulson, L. Lari, M. Isaacs, D.J. Raines, R.E. Douthwaite, A.K. Duhme-Klair, Carbon Nitride as a Ligand: Selective Hydrogenation of Terminal Alkenes Using [(η5-C5Me5)IrCl(g-C3N4-κ2N, N')]Cl. Chem. – A Eur, J. 26 (2020) 6862–6868, https://doi.org/10.1002/CHEM.201905749.

[88] M. Ceotto, L. Lo Presti, G. Cappelletti, D. Meroni, F. Spadavecchia, R. Zecca, M. Leoni, P. Scardi, C.L. Bianchi, S. Ardizzone, About the nitrogen location in nanocrystalline N-doped TiO 2: Combined DFT and EXAFS approach, J. Phys. Chem. C 116 (2012) 1764–1771, https://doi.org/10.1021/JP2097636/SUPPL_FILE/JP2097636_SI_001.PDF.

[89] M. Sahoo, A.K. Yadav, S.N. Jha, D. Bhattacharyya, T. Mathews, N.K. Sahoo, S. Dash, A.K. Tyagi, Nitrogen Location and Ti-O Bond Distances in Pristine and N-Doped TiO2 Anatase Thin Films by X-ray Absorption Studies, J. Phys. Chem. C 119 (2015) 17640–17647, https://doi.org/10.1021/ACS.JPCC.5B03295/SUPPL_FILE/JP5B03295_SI_001.PDF.

[90] L.X. Chen, T. Rajh, Z. Wang, M.C. Thurnauer, XAFS Studies of Surface Structures of TiO $_2$ Nanoparticles and Photocatalytic Reduction of Metal Ions, J. Phys. Chem. B 101 (1997) 10688–10697, https://doi.org/10.1021/jp971930g.

[91] Y. Markushyna, P. Lamagni, J. Catalano, N. Lock, G. Zhang, M. Antonietti, A. Savateev, Advantages in Using Inexpensive CO2 to Favor Photocatalytic Oxidation of Benzylamines, ACS Catal. 10 (2020) 7336–7342, https://doi.org/10.1021/ACSCATAL.0C02176/SUPPL_FILE/CS0C02176_SI_001.PDF.

[92] J.T. Schneider, D.S. Firak, R.R. Ribeiro, P. Peralta-Zamora, Use of scavenger agents in heterogeneous photocatalysis: truths, half-truths, and misinterpretations, PCCP 22 (2020) 15723–15733, https://doi.org/10.1039/D0CP02411B.

[93] A. Savateev, N.V. Tarakina, V. Strauss, T. Hussain, K. ten Brummelhuis, J. M. Sánchez Vadillo, Y. Markushyna, S. Mazzanti, A.P. Tyutyunnik, R. Walczak, et al., Potassium Poly(Heptazine Imide): Transition Metal-Free Solid-State Triplet Sensitizer in Cascade Energy Transfer and [3+2]-cycloadditions, Angew. Chemie - Int. Ed. 59 (2020) 15061–15068, https://doi.org/10.1002/ANIE.202004747.

[94] A. Galushchinskiy, K. ten Brummelhuis, M. Antonietti, A. Savateev, Insights Into the Mechanism of Energy Transfer with Poly(Heptazine Imide)s in a Deoximation Reaction, ChemPhotoChem 5 (2021) 1020–1025, https://doi.org/10.1002/CPTC.202100088.

[95] Y. Markushyna, P. Lamagni, C. Teutloff, J. Catalano, N. Lock, G. Zhang, M. Antonietti, A. Savateev, Green radicals of potassium poly(heptazine imide) using light and benzylamine, J. Mater. Chem. A 7 (2019) 24771–24775, https://doi.org/10.1039/C9TA09500D.

[96] Schneider, J., and Detlef W, B. (2013). Undesired Role of Sacrificial Reagents in Photocatalysis. J. Chem. Lett. *4*, 3479–3483. 10.1021/jz4018199.

[97] M. Wang, S. Shen, L. Li, Z. Tang, J. Yang, Effects of sacrificial reagents on photocatalytic hydrogen evolution over different photocatalysts, J. Mater. Sci. 52 (2017) 5155–5164, https://doi.org/10.1007/s10853-017-0752-z.

[98] M. Chandra, U. Guharoy, D. Pradhan, Boosting the Photocatalytic H2 Evolution and Benzylamine Oxidation using 2D/1D g-C3N4/TiO2 Nanoheterojunction, ACS Appl. Mater. Interfaces 14 (2022) 22122–22137, https://doi.org/10.1021/ACSAMI.2C03230/ASSET/IMAGES/LARGE/AM2C03230_0010.JPEG.

[99] X. Li, S. Lyu, X. Lang, Superoxide generated by blue light photocatalysis of g-C3N4/TiO2 for selective conversion of amines, Environ. Res. 195 (2021) 110851, https://doi.org/10.1016/J.ENVRES.2021.110851.

[100] I. Zizak, The mySpot beamline at BESSY II, J. Large-Scale Res. Facil. JLSRF 2 (2016) A102–A, https://doi.org/10.17815/JLSRF-2-113.

[101] J. Kieffer, D. Karkoulis, PyFAI, a versatile library for azimuthal regrouping, J. Phys. Conf. Ser. 425 (2013) 202012, https://doi.org/10.1088/1742-6596/425/20/202012.

[102] I. Zizak, mySpot: a versatile microfocussing station for scanning methods at BESSY II, J. Large-Scale Res. Facil. JLSRF 2, A101 (2016), https://doi.org/10.17815/jlsrf-2-115.

[103] B. Ravel, M. Newville, ATHENA, ARTEMIS, HEPHAESTUS : data analysis for X-ray absorption spectroscopy using IFEFFIT, J. Synchrotron Radiat. 12 (2005) 537–541, https://doi.org/10.1107/S0909049505012719.